Supplementary Information

Enhancing Lithium Storage Rate and Durability in Sphalerite GeP by Engineering Configurational Entropy

Yanhong Li,[a, c] Jeng-Han Wang,[b] Tzu-Yu Liu,[b] Xinwei Li,[e] Zaiping Guo,[d] Meilin Liu,[a] and Wenwu Li,[a, e, *]

Dr. Yanhong Li, Prof. Meilin Liu, Prof. Wenwu Li
[a] School of Materials Science & Engineering, Georgia Institute of Technology, Atlanta, GA 30332, USA

Prof. Jeng-Han Wang, Tzu-Yu Liu
[b] Department of Chemistry, National Taiwan Normal University, Taipei, 11677, Taiwan

Dr. Yanhong Li
[c] Faculty of Materials Science and Engineering/Institute of Technology for Carbon Neutrality, Shenzhen Institute of Advanced Technology, Chinese Academy of Sciences Shenzhen 518060, China

Prof. Zaiping Guo
[d] School of Chemical Engineering & Advanced Materials, The University of Adelaide Adelaide, SA 5005, Australia

Dr. Xinwei Li, Prof. Wenwu Li
[e] School of Chemical Engineering, Sungkyunkwan University, 2066, Seoburo, Jangan-gu, Suwon 440-746, Republic of Korea. Email: wenwuli@skku.edu

Keywords: High Conformational Entropy; Sphalerite Lattice; Metallic Conductivity; Germanium-Phosphides Anodes; Li-ion batteries

1. Supplemental Methods:

Method S1: The calculation of configurational entropy

Configurational entropy is calculated by the following equation:[1-3]

$$\Delta S_{conf} = -R\left[\left(\sum_{i=1}^{n} x_i \ln x_i\right)_{cation\ site} + \left(\sum_{j=1}^{n} x_j \ln x_j\right)_{anion\ site}\right] (1).$$

In this equation, x_i denotes the fraction of the element component, ln represents natural logarithm function, $\sum_{i=1}^{n} x_i$ is applied to summation over the element component. R is the gas constant. ΔS_{conf} represents the change in configurational entropy. As a consequence, based on the equation (1), all the configurational entropy is showed in **Figure 5** and **7**.

Method S2: The calculation of the lithium-ion diffusion coefficients

The lithium-ion diffusion coefficients (D) is measured by using the Galvanostatic Intermittent Titration Technique (GITT) as following:[4, 5] $D = \frac{4}{\pi\tau}\left(\frac{n_m V_m}{S}\right)^2 \left(\frac{\Delta E_s}{\Delta E_t}\right)^2$ (t<<$\frac{L^2}{D}$) (2)

In this equation, D represents the lithium-ion diffusion coefficient, $\frac{4}{\pi\tau}$ represents a factor accounting for the experimental time scale, V_m, is the molar volume of the material, S Represents the surface area of the electrode or the area through which the lithium ions diffuse, E_s, is the change in potential during the discharge (or charge) process, ΔE_t, represents the total change in potential throughout the entire experiment, t represents the time interval over which the voltage changes during the GITT experiment, L denotes the thickness of the electrode material through which lithium ions are diffusing.

Method S3: Calculations details

The Vienna Ab-initio Simulation Package (VASP) was utilized for performing density functional theory (DFT) calculations.[6] The computational method employed was at the GGA-PW91 level, utilizing the exchange-correlation functional with generalized gradient approximation in the Perdew-Wang 1991 formulation.[7] Planewaves were used as the basis set with a cutoff energy of 600 eV for valence electrons, while cost-effective pseudopotentials

were employed to simulate core electrons. Brillouin zone integrations were performed using the Monkhorst-Pack scheme in reciprocal space with an interval of 0.05×2 (Å^{-1}).[8]

Initially, supercells of $Zn_{24}Ge_{24}Si_{24}P_{72}$, $Ge_{12}P_{12}$, and $Si_{24}P_{24}$ were constructed to simulate $ZnGeSiP_3$, layered GeP, and SiP, respectively. These structures were fully optimized without constraints, and their energies were computed using the quasi-Newton method with energy and gradient convergence criteria set at $1×10^{-4}$ eV and $1×10^{-2}$ eV Å^{-1}, respectively. The resulting energies were then used to examine their formation energies from pure elements, calculated as the difference between the energy of the compound and the energies of its constituent elements. i.e. formation energy of $ZnGeSiP_3$ = E($ZnGeSiP_3$) – E(Zn) – E(GeP) – E(SiP) – E(P)= E($ZnGeSiP_3$) – E(Zn) – E(Ge) – E(Si) – 3E(P) = E($ZnGeSiP_3$) – E(Zn) – E(GeP) – E(Si) – 2E(P) = E($ZnGeSiP_3$) – E(Zn) – E(Ge) – E(SiP) – 2E(P)

The optimized structures were further employed for the analysis of density of states (DOS), vibrational modes, Young's modulus, and induced charges. In the DOS analysis, the s, p, and d bands of each element were decomposed. The finite displacement approach, involving slight displacements of atoms in the optimized structures to calculate the forces on each atom,[9] was used to derive the Hessian matrix for analyzing vibrational modes. Induced charge was determined as the difference between the charge distribution at the optimized structure and that at the elemental state without chemical bonding.

Additionally, Li adsorption on $ZnGeSiP_3$, GeP, and SiP was investigated, forming Li-$ZnGeSiP_3$, Li-GeP, and Li-SiP. Their structures were fully optimized, and energies were computed to determine the adsorption energy. The barriers for Li diffusion on different sites were calculated using the nudged elastic band (NEB) method to locate the transition states with

the same energetic and gradient convergences.[10]
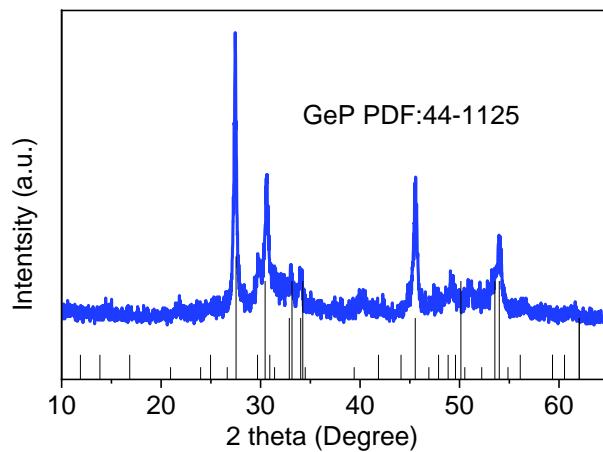
2. Supplementary Figures

Figure S1. X-ray diffraction (XRD) pattern of layer GeP, used for synthesis.
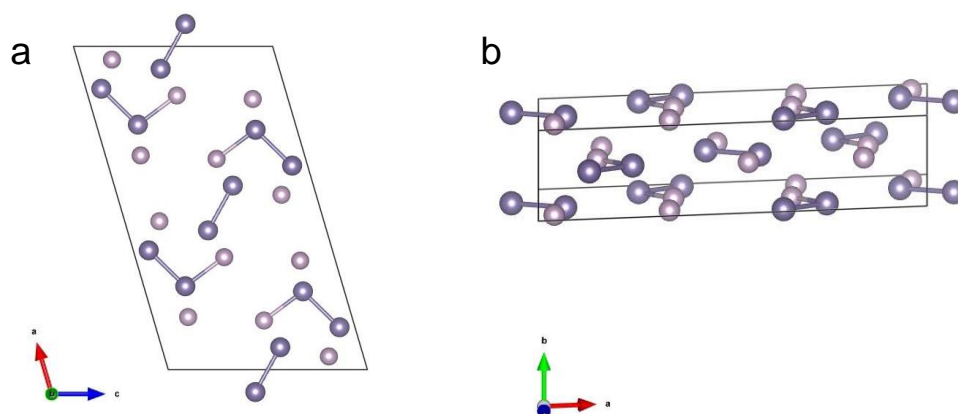

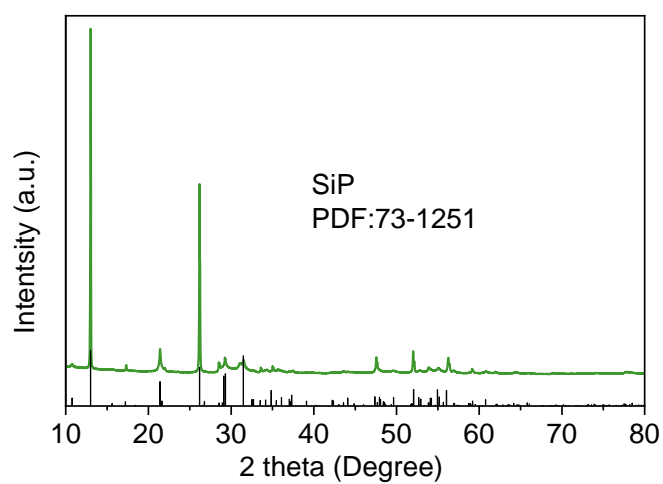**Figure S2.** Crystal structure diagram of layer GeP, used for calculations.

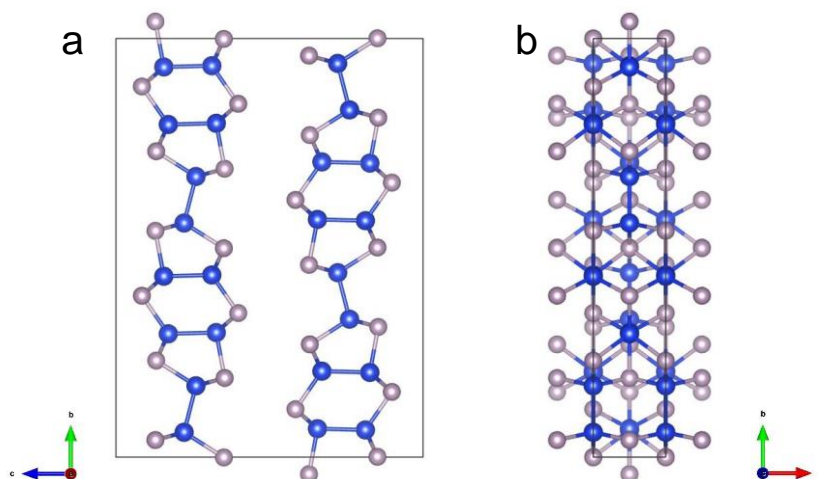**Figure S3.** XRD patterns of layer SiP, used for synthesis.

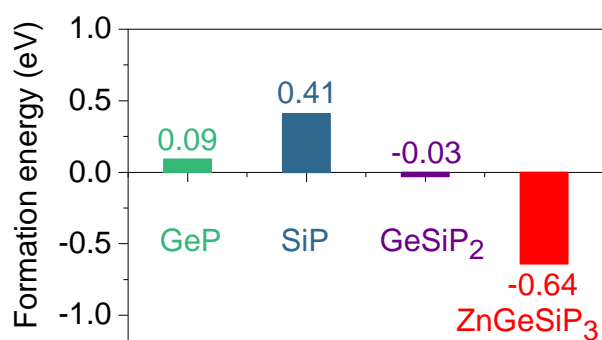**Figure S4.** Crystal structure diagram of layer SiP, used for calculations.

Figure S5. Formation energies of sphalerite-structured compounds including GeSiP$_2$, GeP, and SiP.
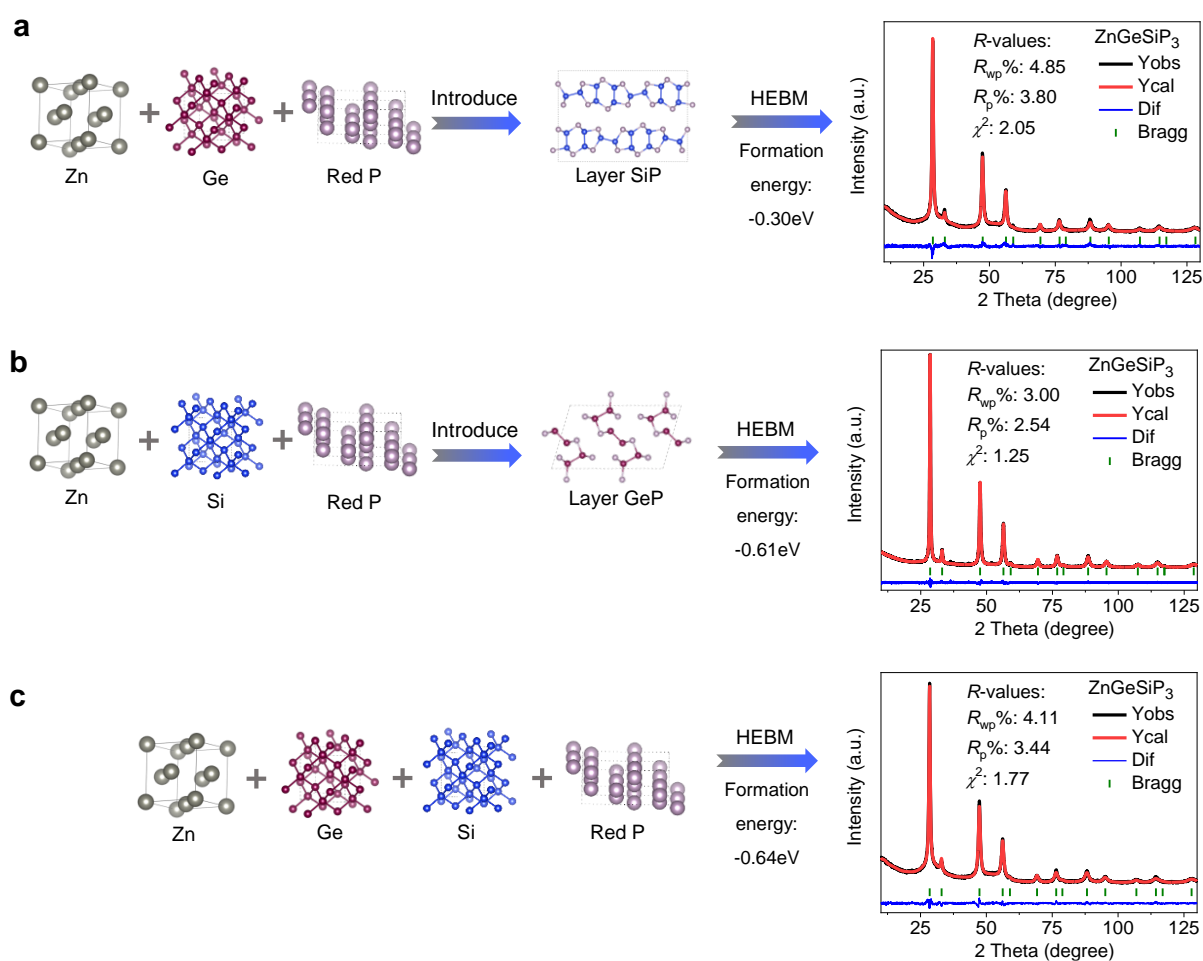

Figure S6. Illustrated preparation schemes and the associated formation energies of the sphalerite-structured GeP-based compound ZnGeSiP$_3$ utilizing diverse reaction paths with distinct raw materials. These include: (a) Raw materials SiP, Ge, Zn, and P; (b) Raw materials GeP, Si, Zn, and P; (c) Raw materials Ge, P, Si, and Zn.
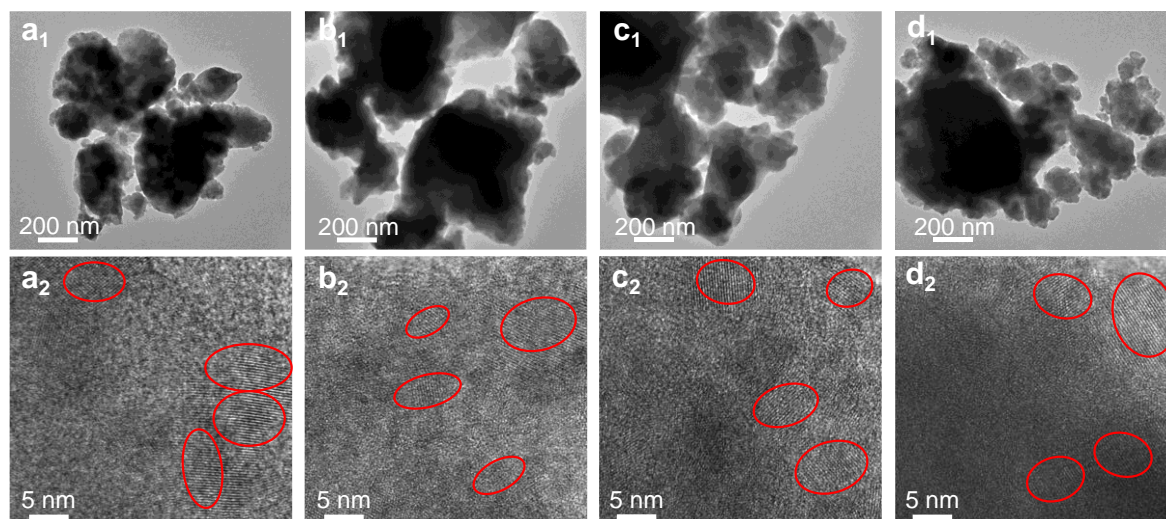
Figure S7. Low magnification and high-resolution TEM images of ZnGeSiP$_3$ by using different raw materials.
(a) Raw materials of layer GeP and layer SiP, Zn, and P.
(b) Raw materials of layer SiP, Ge, Zn, and P.
(c) Raw materials of layer GeP, Si, Zn, and P.
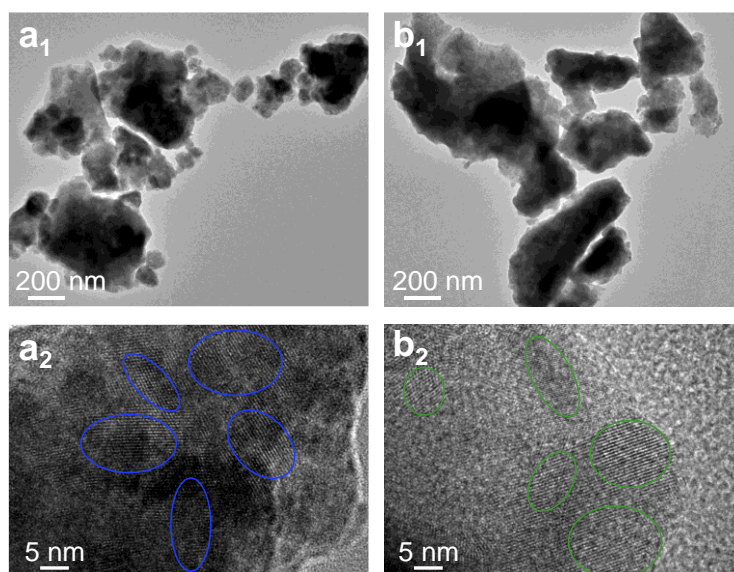(d) Raw materials of Ge, Si, Zn and P.

Figure S8. Transmission electron microscopy (TEM) images.
(a) layer GeP.
(b) layer SiP.

As depicted in **Figure 1a-b** and **S6**, after 10 h of ball milling, the X-ray diffraction (XRD) patterns of the four samples using different precursors exhibited minimal differences in terms of peak intensity and full width at half maximum (FWHM). This similarity indicates that macroscopically, they are very alike. We also conducted transmission electron microscopy (TEM) tests. At low magnification (**Figure S7a$_1$-d$_1$**), these four samples exhibit similar

morphological features, appearing as typical ball-milled aggregates with secondary particles at the micrometer scale. Further high-resolution TEM analysis (**Figure S7a₂-d₂**) indicated that they possess similar crystal sizes, consistent with the XRD results.

Note that all compounds were synthesized under identical ball milling conditions. Therefore, compared to the layered Ge (or Si)P precursors, they exhibit similar morphological features and crystallinity, as shown by both low-magnification (**Figure S8a₁-b₁**) and high-magnification TEM (**Figure S8a₂-b₂**) images.
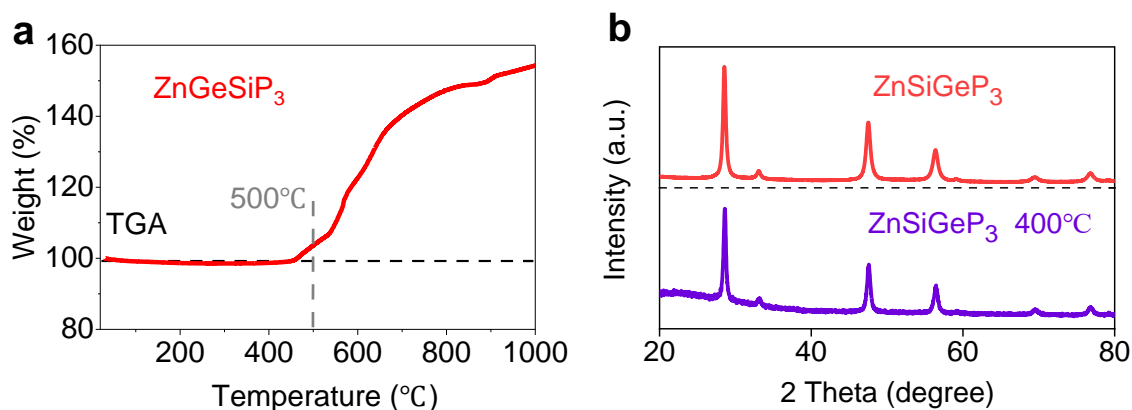

Figure S9. (a) Thermogravimetric and differential thermal analysis (TG-DTA) curve of the sphalerite-structured GeP-based compound $ZnGeSiP_3$. (b) XRD patterns of the pristine sphalerite-structured GeP-based compound $ZnGeSiP_3$ powder and the $ZnGeSiP_3$ annealed for 5 hours in air.
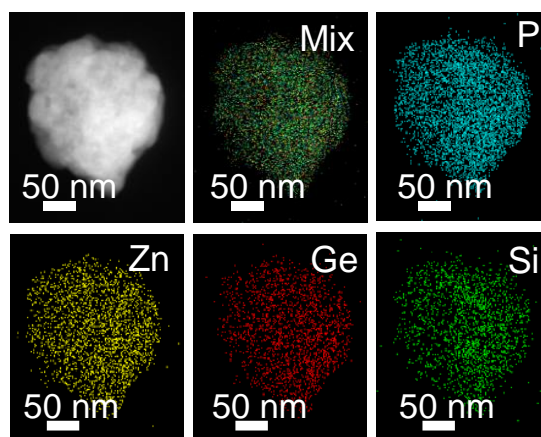

Figure S10. Elemental mappings of the sphalerite-structured GeP-based compound $ZnGeSiP_3$.
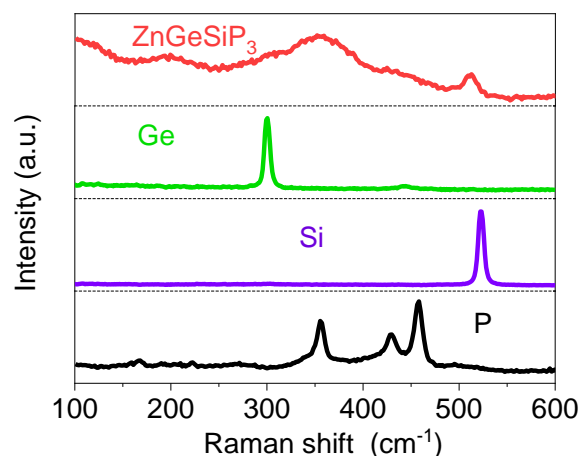
Figure S11. Raman spectra of the sphalerite-structured GeP-based compound ZnGeSiP$_3$, Ge, Si, and P.
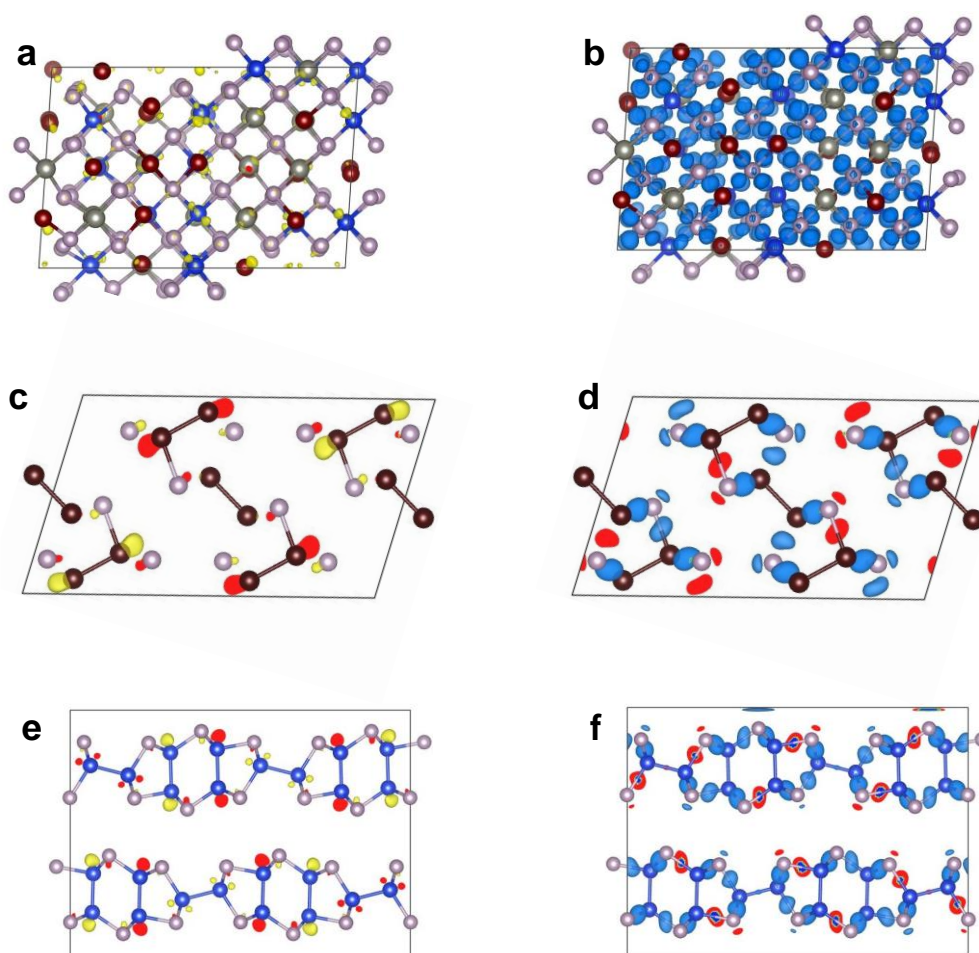

Figure S12. (a-b) Positive and negative charge distributions of the sphalerite-structured GeP-based compound ZnGeSiP$_3$.
(c-d) Positive and negative charge distributions of layer GeP.
(e-f) Positive and negative charge distributions of layered SiP.
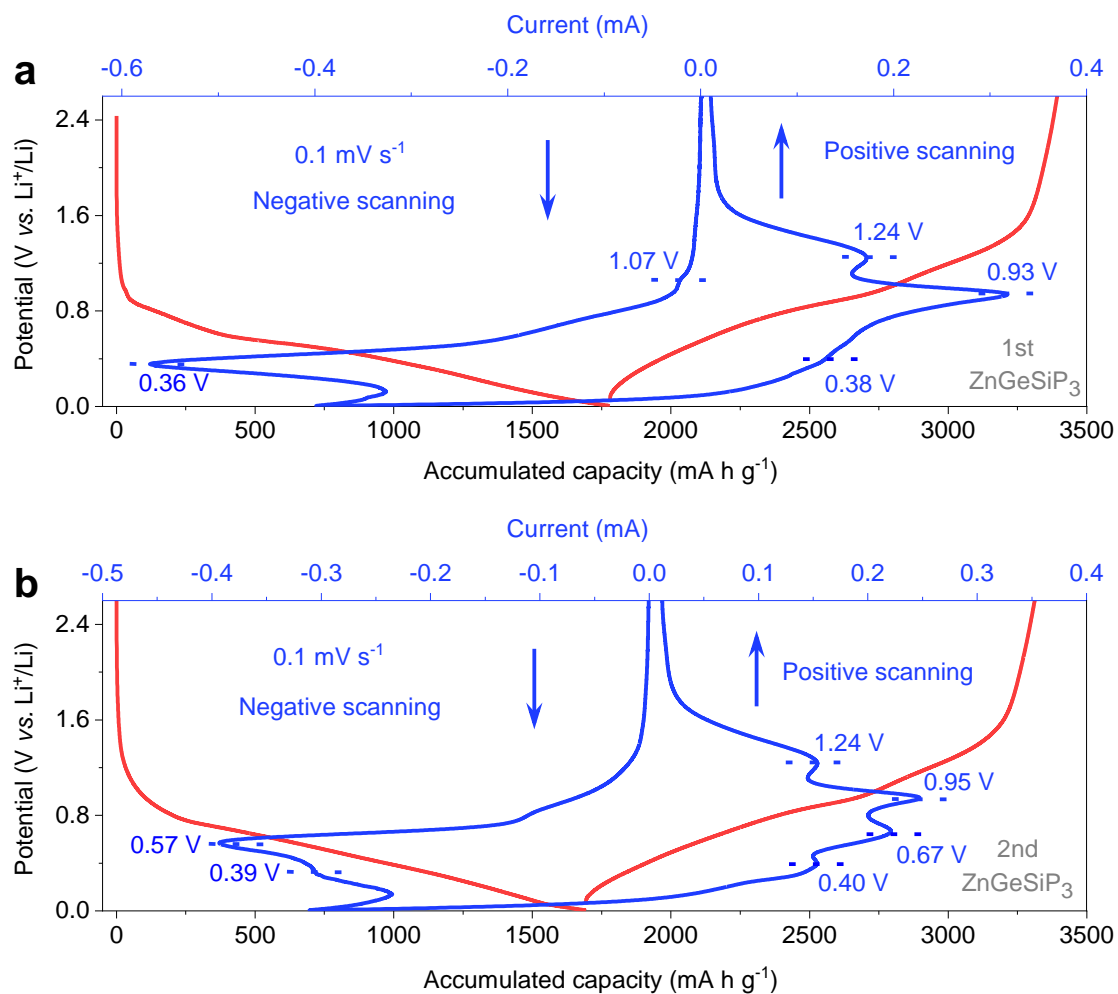Total charge distributions are shown in **Fig. 1k-m**.

Figure S13. (a) Merged profile of the first galvanostatic charge-discharge (GCD) and cyclic voltammetry (CV). (b) Merged profile of the second GCD and CV.
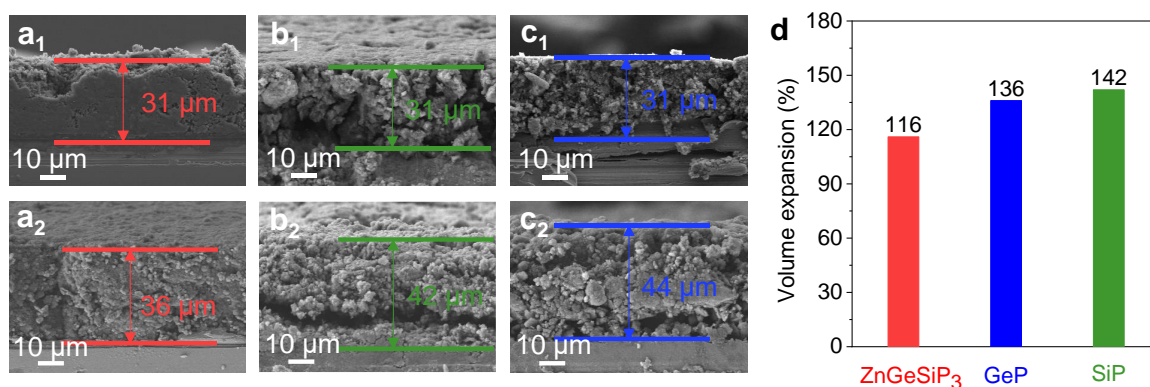

Figure S14. Electrode cross-section SEM images: pristine vs. post-cycling.
(a) $ZnGeSiP_3$.
(b) Layer GeP.
(c) Layer SiP.
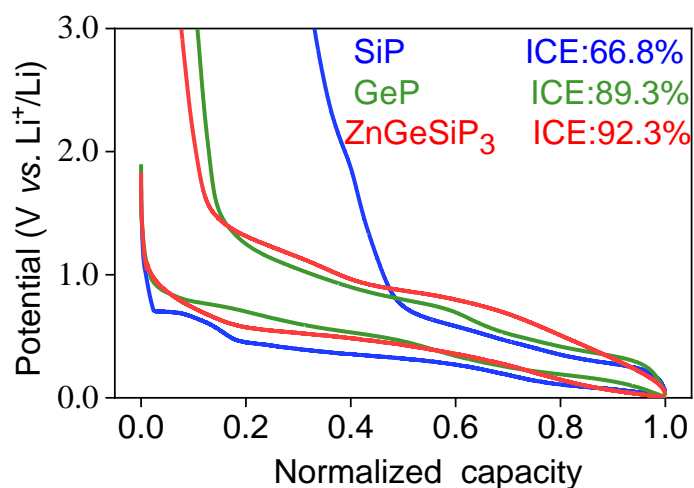(d) Volume expansion rate.

Figure S15 Initial GCD profiles of the sphalerite-structured ZnGeSiP$_3$ and layered GeP (or SiP).
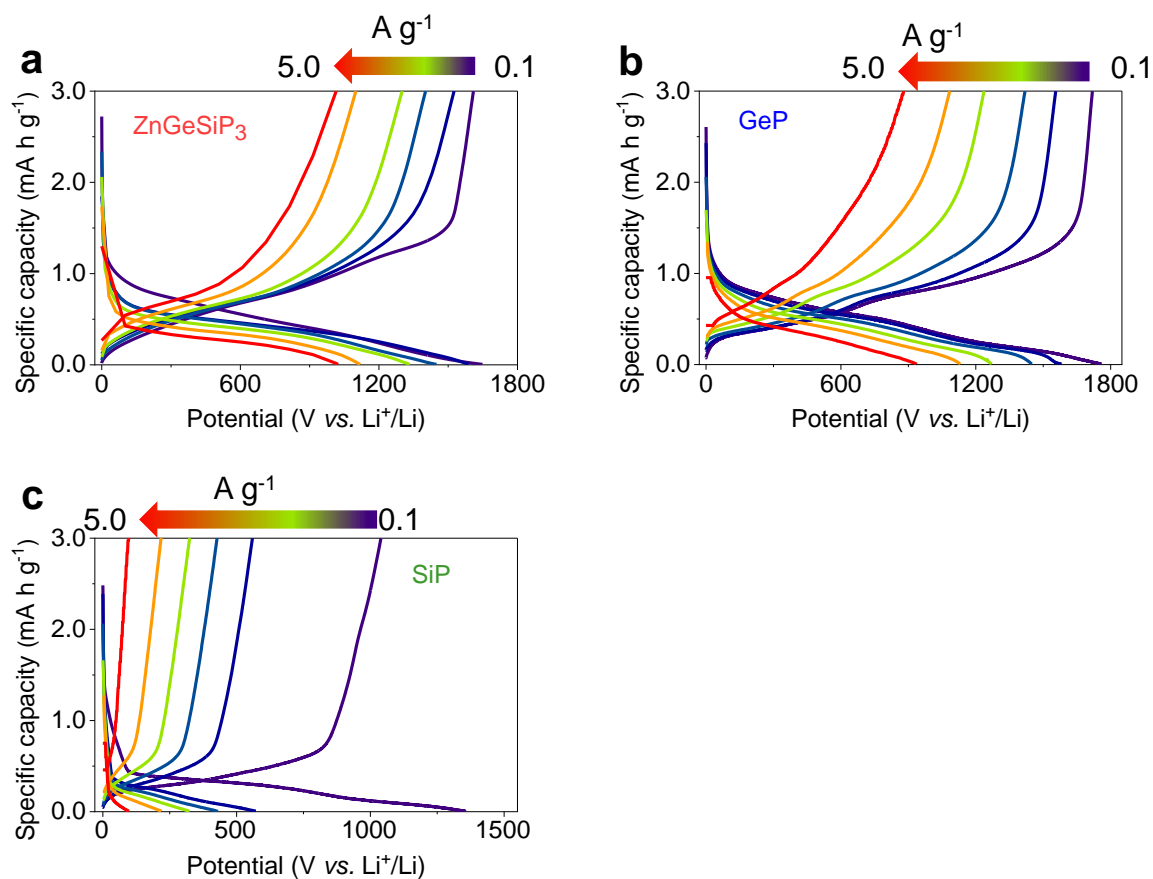
Figure S16. The GCD profiles under various current rates.
(a) Sphalerite-structured ZnGeSiP$_3$ compound.
(b) Layered GeP.
(c) layered SiP.
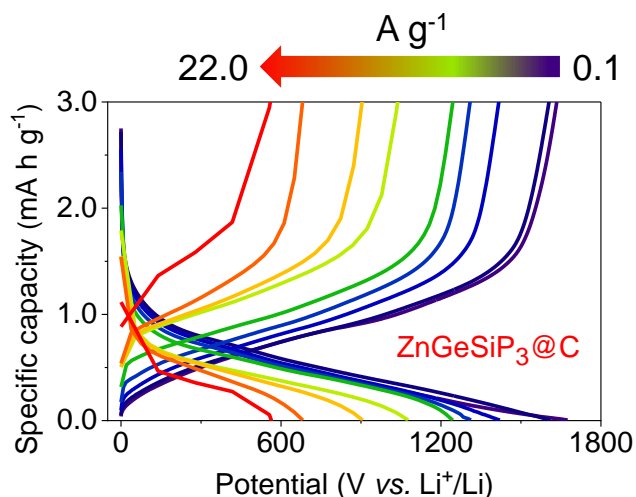
Figure S17. The GCD profiles of the sphalerite-structured ZnGeSiP$_3$@C at different current rates.
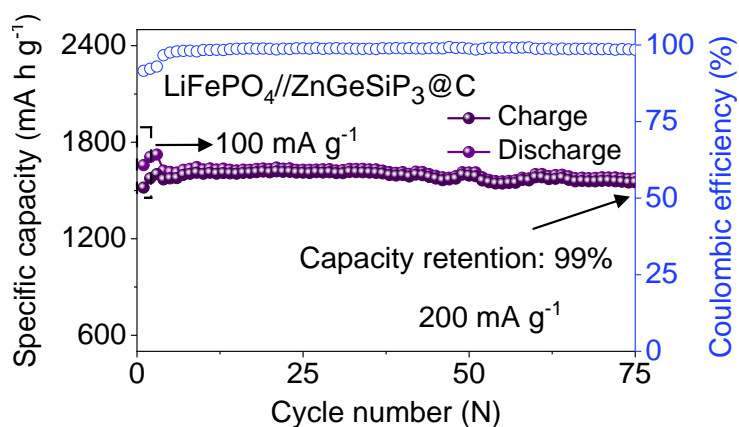
Figure S18. LiFePO$_4$//ZnGeSiP$_3$@C full-cell.
Cycle performance.
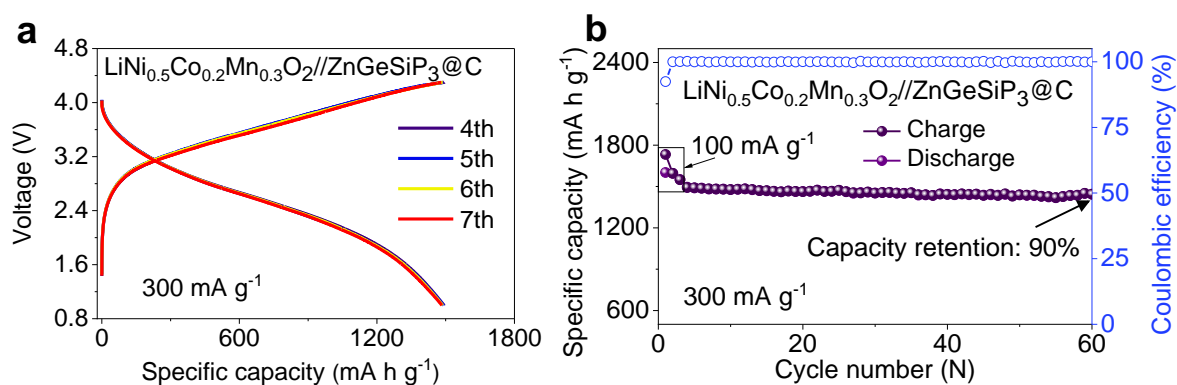
Figure S19. Electrochemical performances of LiNi$_{0.5}$Co$_{0.2}$Mn$_{0.3}$O$_2$//ZnGeSiP$_3$@C full-cell.
(a) Galvanostatic charge-discharge (GCD) profiles.
(b) Cycle performance.
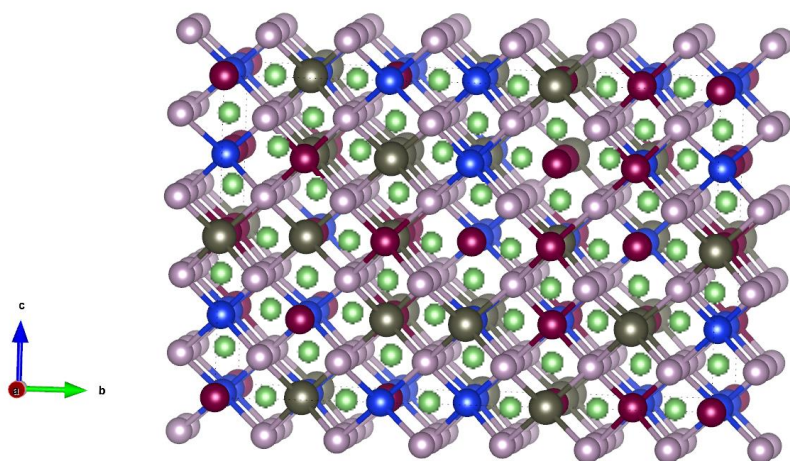
Figure S20. Supercell models of Li₃ZnGeSiP₃.
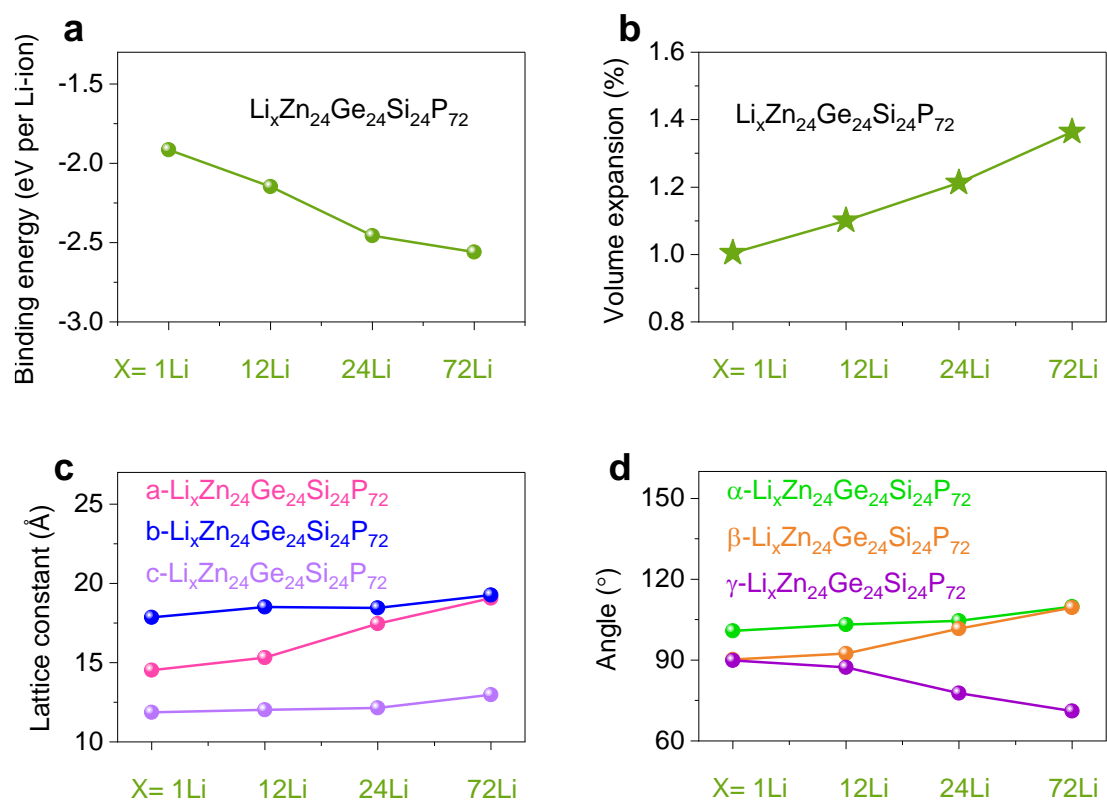
Figure S21. Structural evolution parameters of ZnGeSiP₃ after intercalation by different amounts of Li-ions
(a) Binding energy.
(b) Volume expansion.
(c) Lattice constant.
(d) Angle
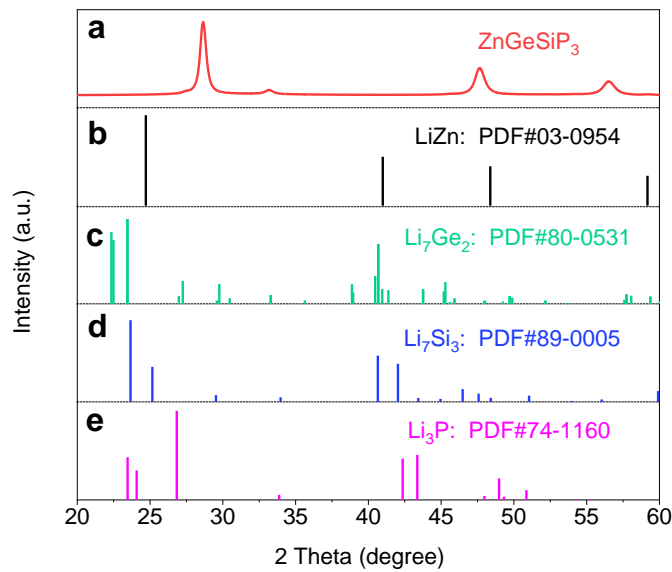
Figure S22. Standard XRD patterns for LiZn, Li$_7$Ge$_2$, Li$_7$Si$_3$, Li$_3$P in Li-storage mechanisms of ZnGeSiP$_3$.
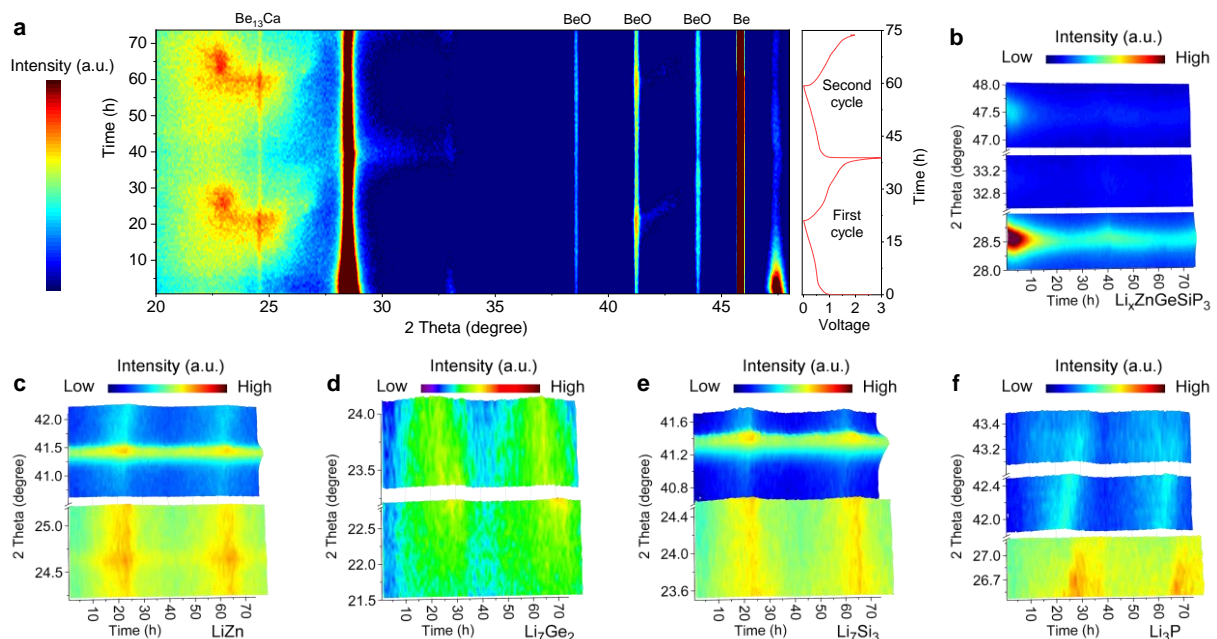
Figure S23. Li-storage mechanisms characterizations of ZnGeSiP$_3$. (Second in-situ XRD)
(a) 2D contour plots of operando XRD during the initial two cycles.
(b-f) XRD pattern evolution of the ZnGeSiP$_3$, LiZn, Li$_7$Ge$_2$, Li$_7$Si$_3$, and Li$_3$P.

To demonstrate the reversible Li-storage mechanisms of ZnGeSiP$_3$, as shown in **Fig. S23**, another set of Operando XRD test was conducted. During this test, the amount of conductive carbon black was reduced to 5%, resulting in clearer signals without interference from carbon black. The lithiation/delithiation processes observed were highly consistent with the first in-situ XRD results (**Fig. 3**) in the manuscript, confirming the reliable Li-storage mechanisms reproducibility of ZnGeSiP$_3$.

14
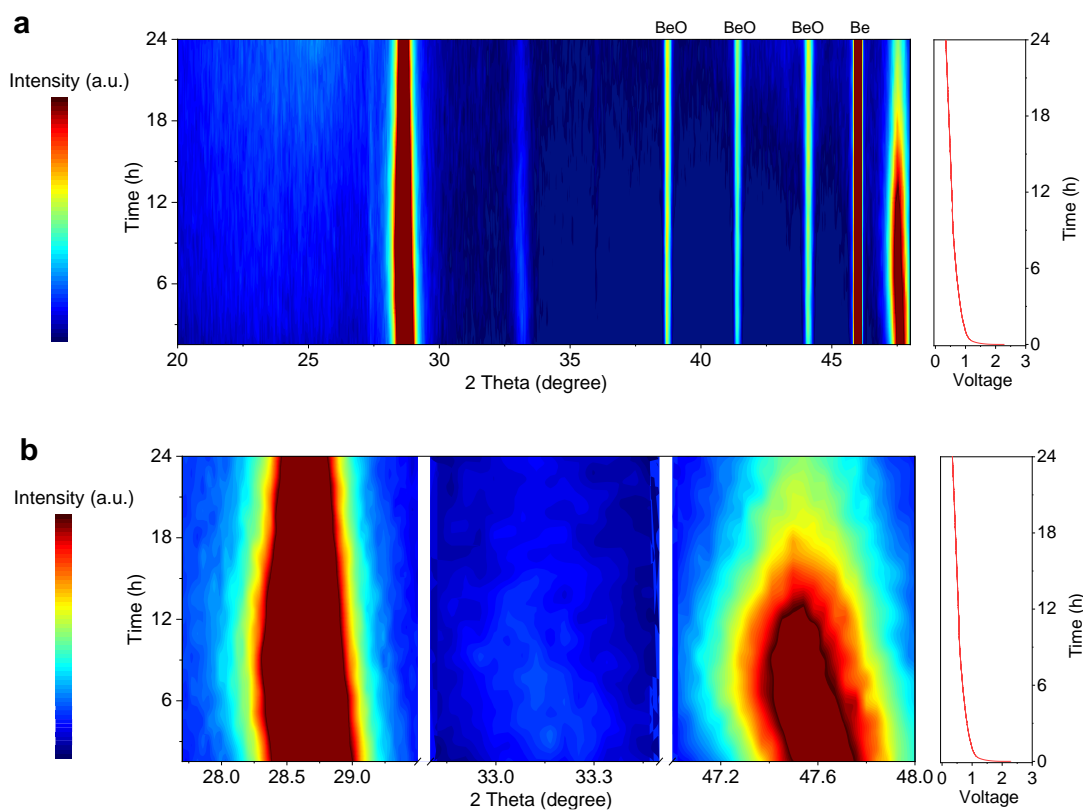
Figure S24. 2D contour plots of operando XRD. (Third in-situ XRD)
(a-b) Evolution of the $ZnGeSiP_3$ during the initial intercalation process.

As shown in **Fig. S24a**, no alloys appear at the very early stage of the intercalation process. It is clearly observed that during the gradual discharge process, the characteristic peaks of $ZnGeSiP_3$ gradually shift towards lower angles (**Fig. S24b**), indicating the gradual intercalation of lithium ions.
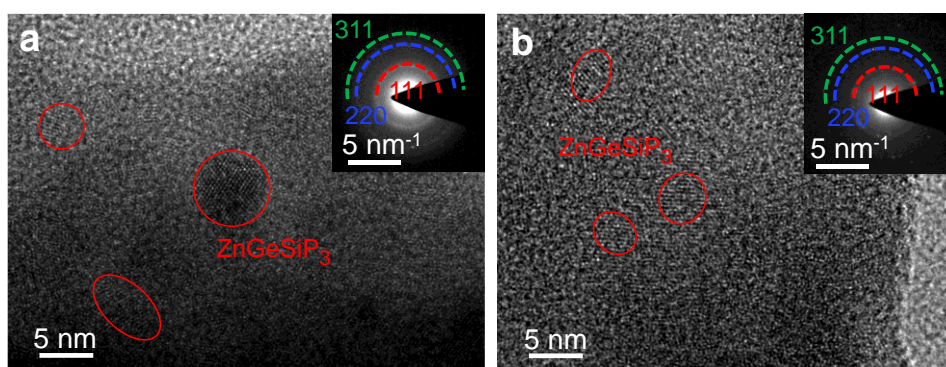
Figure S25. Ex-situ high-resolution transmission electron microscope (HRTEM) and selected area electron diffraction (SAED) of $ZnGeSiP_3$ after cycling.
(a) After 1st cycling.
(b) After10th cycling.
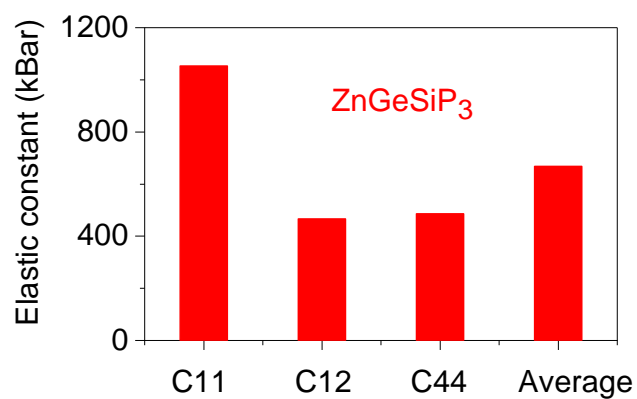
Figure S26. Elastic constant of the sphalerite-structured ZnGeSiP$_3$.
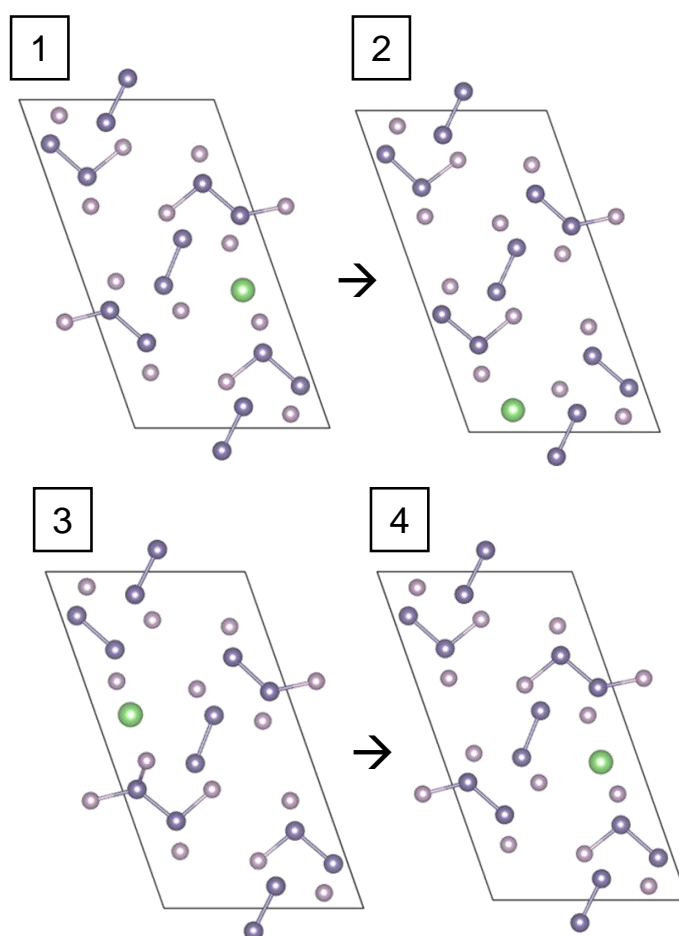
Figure S27. Li-ion diffusion pathways diagram of layered SiP. Corresponding diffusion energy barrier is shown in **Fig. 4b**.
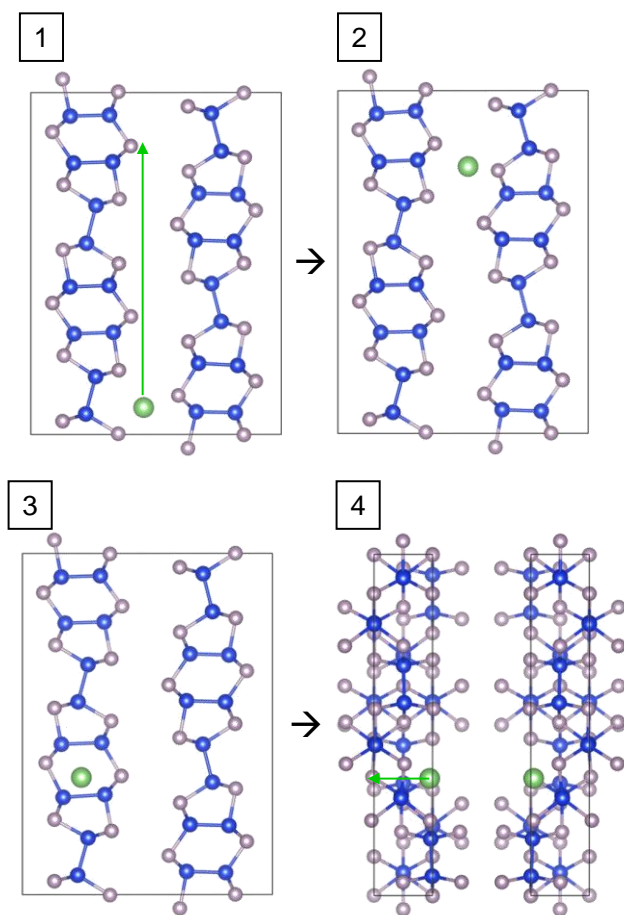
Figure S28. Li-ion diffusion pathways diagram of layered GeP. Corresponding diffusion energy barriers are shown in **Fig. 4b**.
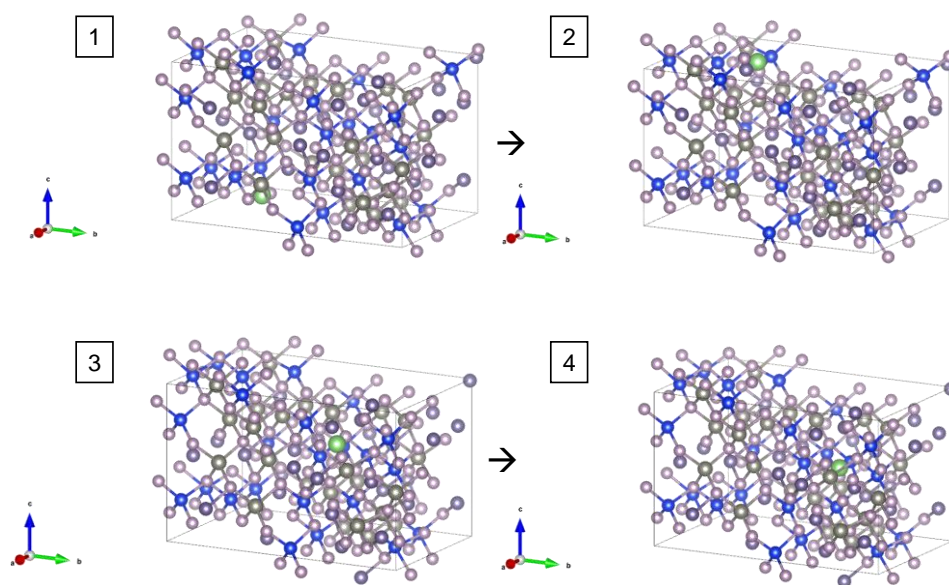
Figure S29. Li-ion diffusion pathways diagram of the sphalerite-structured GeP-based compound ZnGeSiP$_3$. Corresponding diffusion energy barriers are shown in **Fig. 4b**.
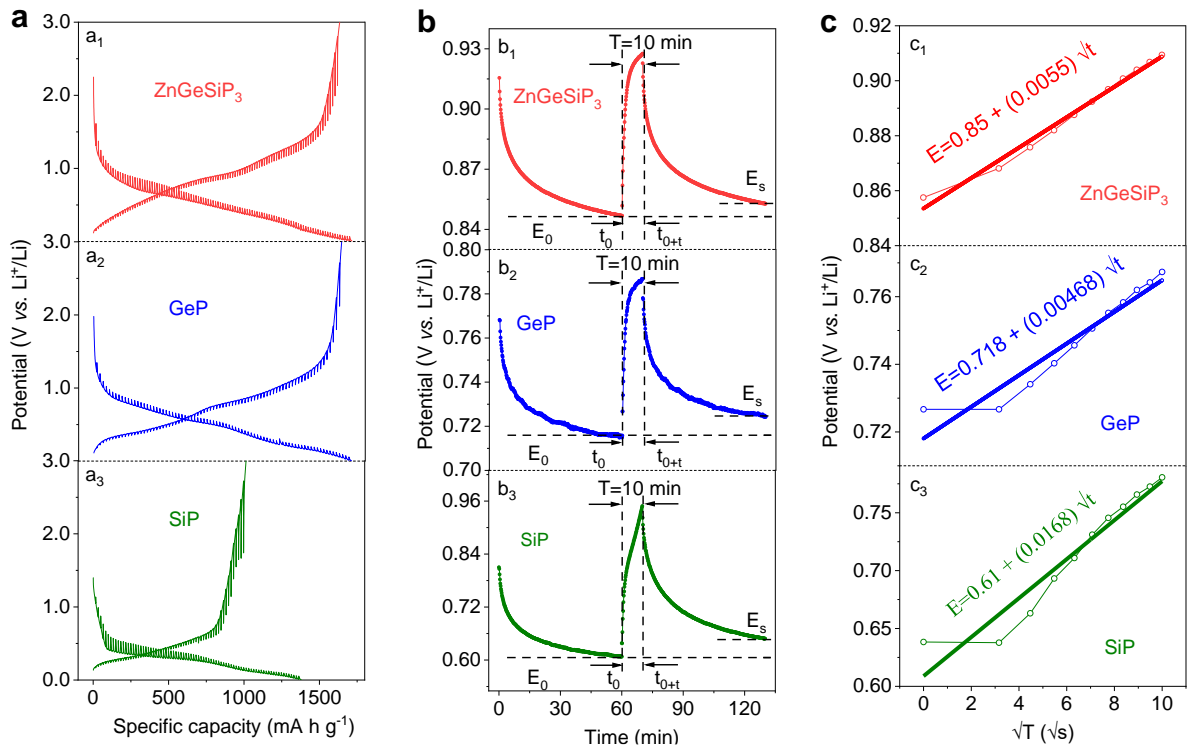
Figure S30. GITT measurement of sphalerite-structured GeP-based compound ZnGeSiP$_3$, and layer Ge(or Si)P.

(a) Potential *vs.* capacity curves at 100 mA g^{-1} with a pulse time of 10 min., and a relaxation time of 1 h.

(b) Detailed potential response over time during a single step of GITT test.

(c) Linear fit of E *vs.* √t in the first 100 s.
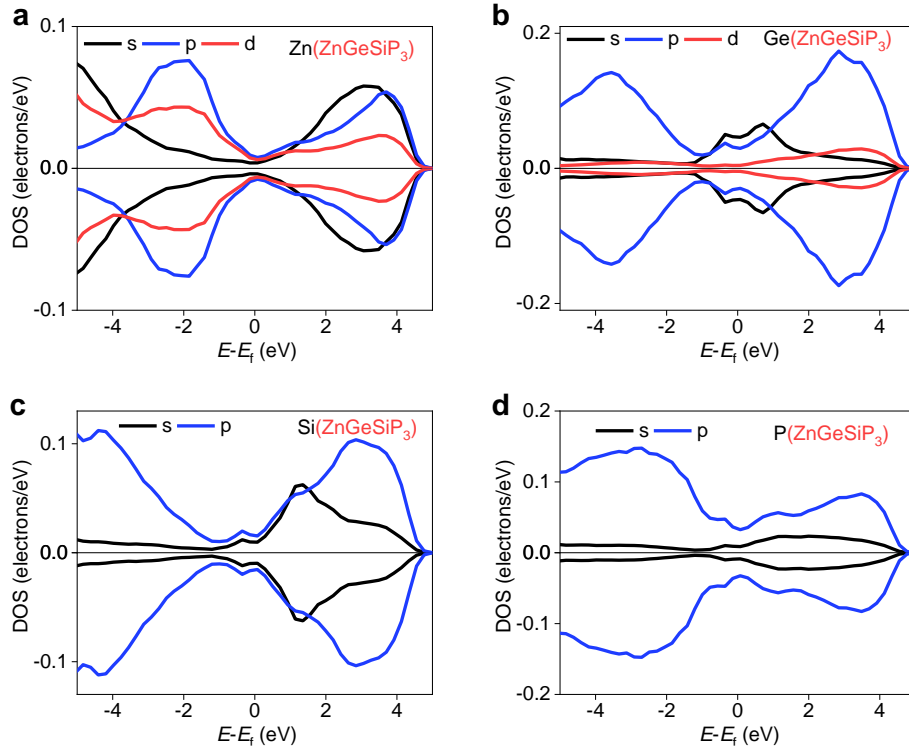
Figure S31. Partial density of states (PDOS) of sphalerite-structured GeP-based compound ZnGeSiP$_3$.
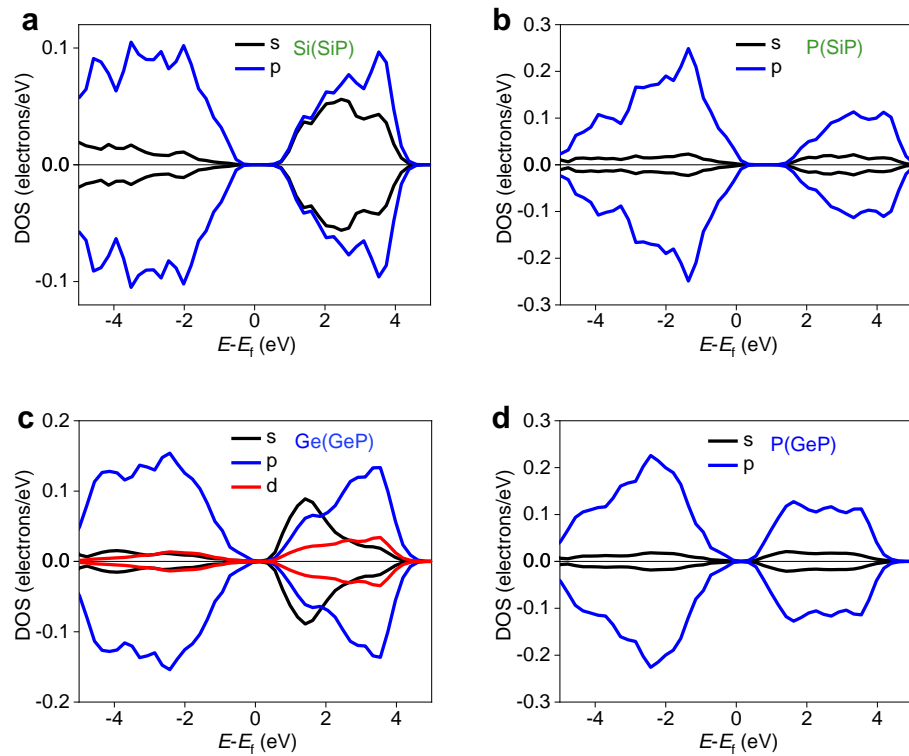
Figure S32. Partial density of states (PDOS) of layered compounds.

(a-b) PDOS of layer SiP.

(c-d) PDOS of layer GeP.
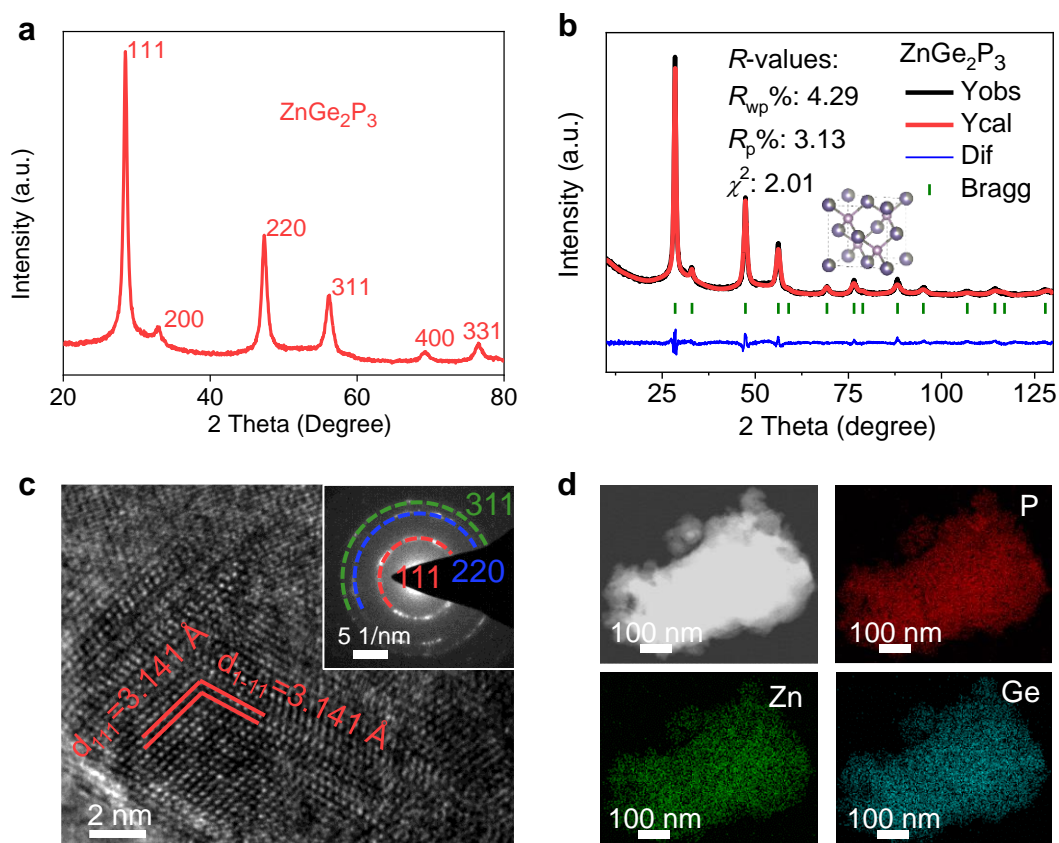
Figure S33. Sphalerite-structured ZnGe₂P₃ compound characterizations.
(a) XRD pattern.
(b) XRD refinement.
(c) HRTEM and SAED.
(d) Elemental mapping.
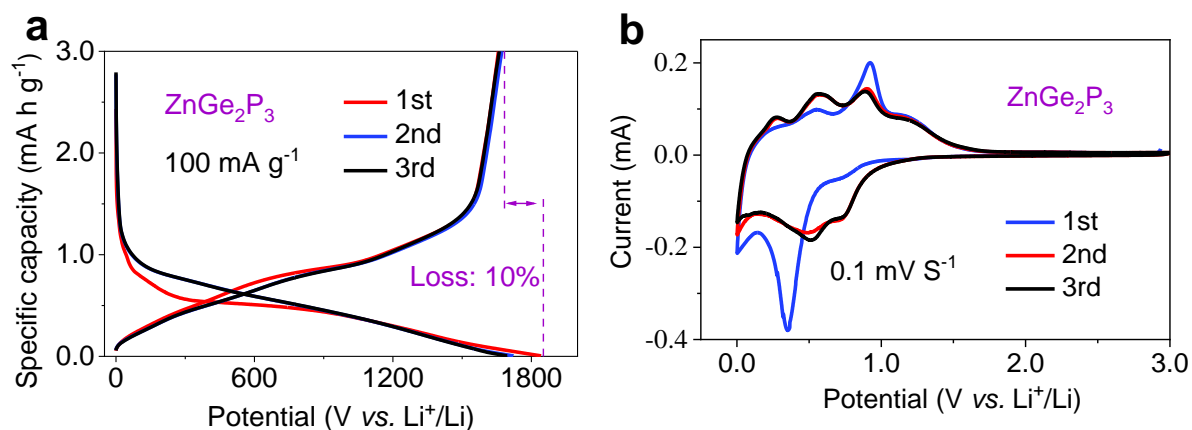
Figure S34. Electrochemical characterizations of the sphalerite-structured GeP-based compound ZnGe₂P₃.
(a) Initial three GCD profiles at 100 mA g⁻¹.
(b) Initial three CV at the scanning rate of 0.1 mV s⁻¹.
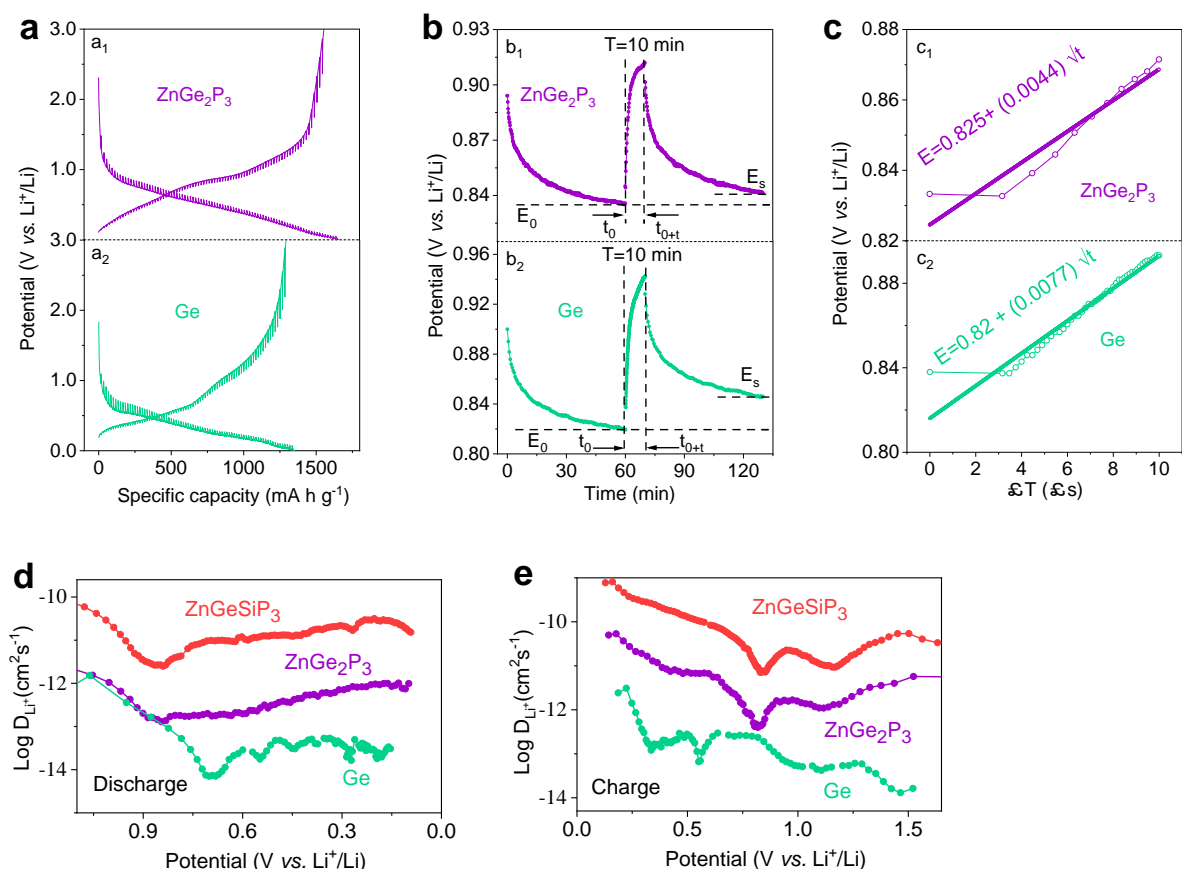
Figure S35. GITT measurement of the sphalerite-structured GeP-based compounds of ZnGeSiP₃ and ZnGe₂P₃, as well as diamond-structured Ge.

(a) Potential *vs.* capacity curves at 100 mA g^{-1} with a pulse time of 10 min., and a relaxation time of 1 h.

(b) Detailed potential response over time during a single step of GITT test.

(c) Linear fit of E vs. √t in the first 100 s.

(d-e) Li-ion diffusion coefficient.
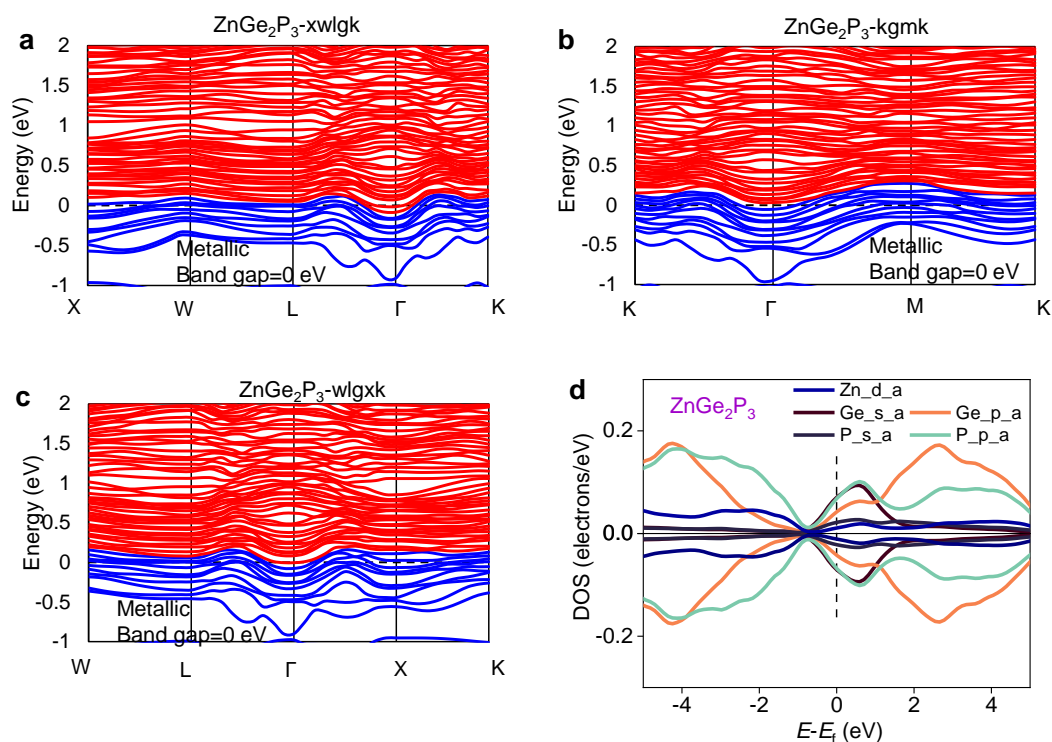
Figure S36. Electronic structures of sphalerite-structured GeP-based compound ZnGe₂P₃.
(a-c) Band structures.
(d) DOS profiles.
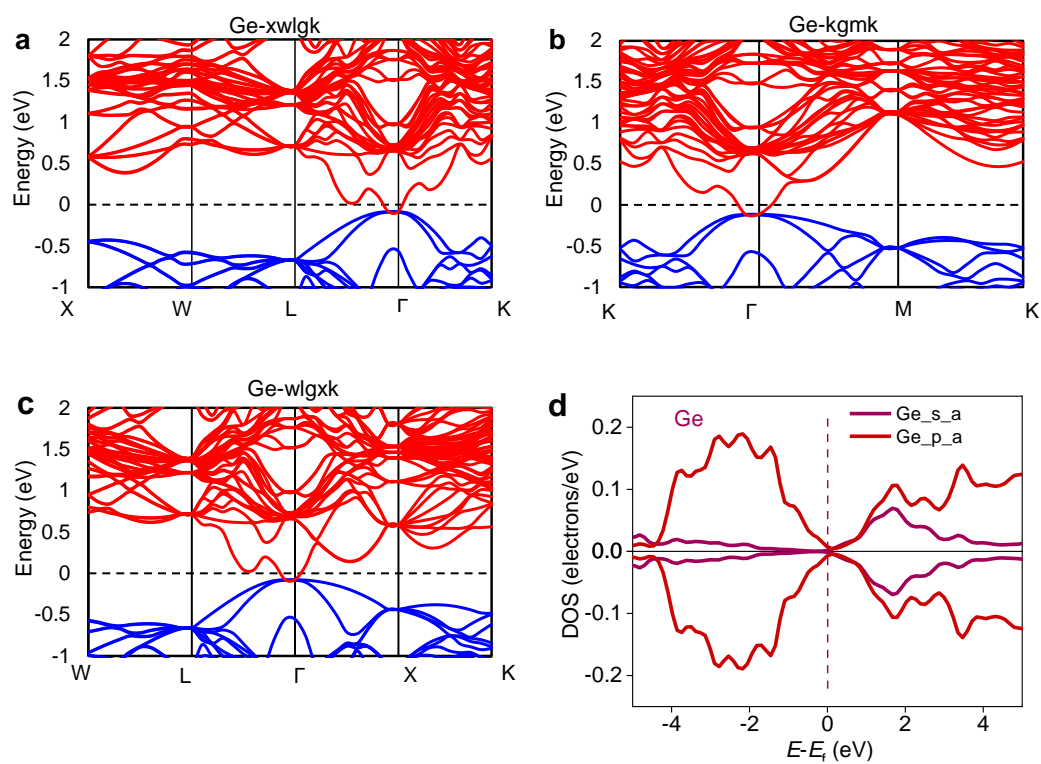
Figure S37. Electronic structures of diamond-structured Ge.
(a-c) Band structures.
(d) DOS profiles.
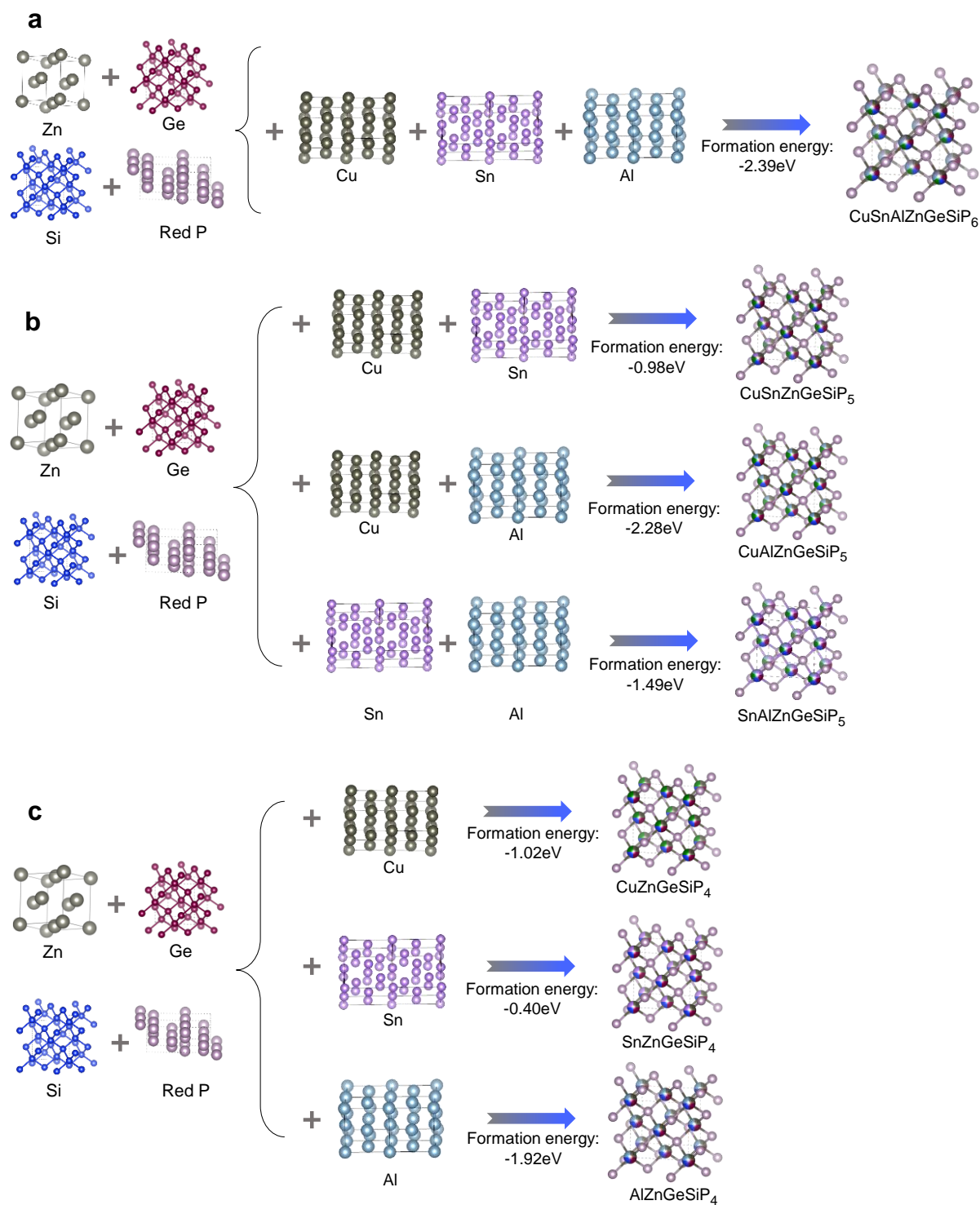
Figure S38. Structural diagram applied to calculate phase formation energies of disordered-cation cubic GeP-based compounds.

(a) CuSnAlZnGeSiP$_6$.

(b) CuSn(or Al)ZnGeSiP$_5$ and SnAlZnGeSiP$_5$.

(c) Cu(or Sn, or Al)ZnGeSiP$_4$.
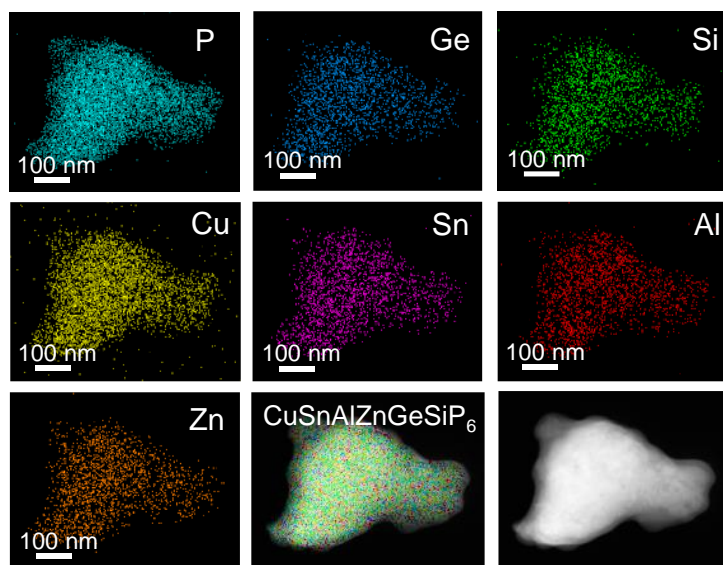
Figure S39. Elemental mappings of the sphalerite-structured GeP-based compound CuSnAlZnGeSiP$_6$.
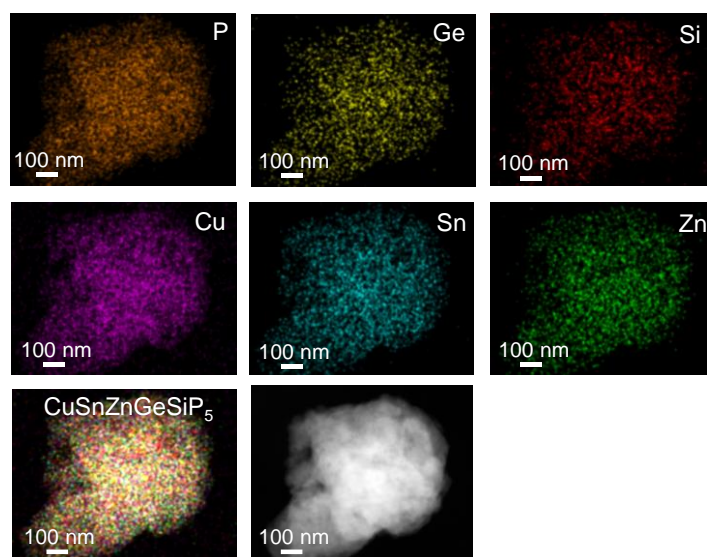
Figure S40. Elemental mappings of the sphalerite-structured GeP-based compound CuSnZnGeSiP$_5$.
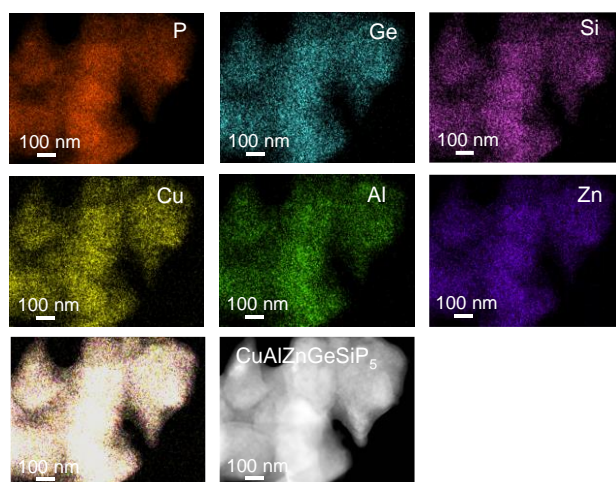
Figure S41. Elemental mappings of the sphalerite-structured GeP-based compound CuAlZnGeSiP$_5$.
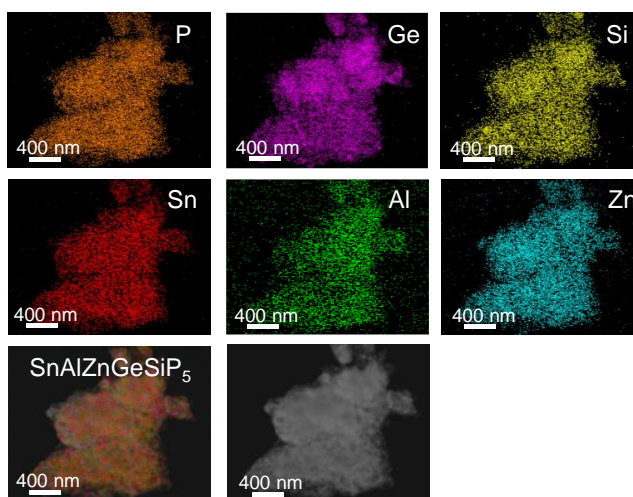
Figure S42. Elemental mappings of the sphalerite-structured GeP-based compound SnAlZnGeSiP$_5$.
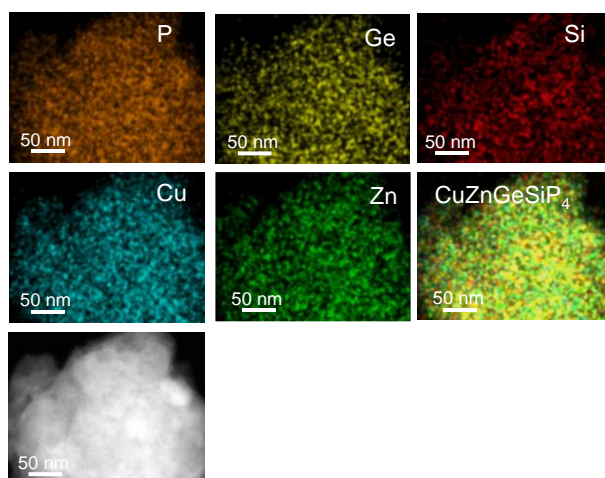
Figure S43. Elemental mappings of the sphalerite-structured GeP-based compound CuZnGeSiP$_4$.
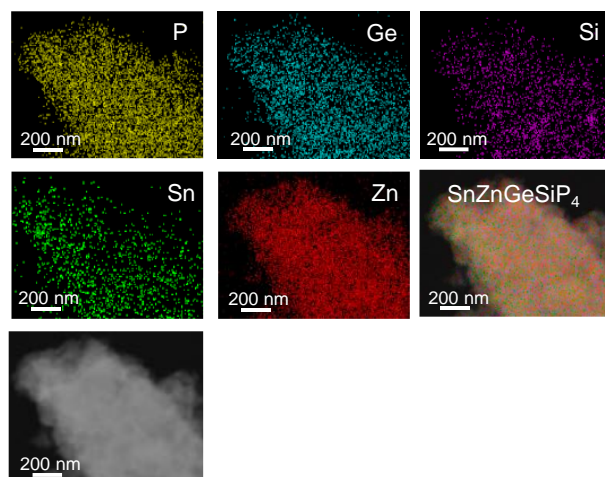
Figure S44. Elemental mappings of the sphalerite-structured GeP-based compound SnZnGeSiP$_4$.
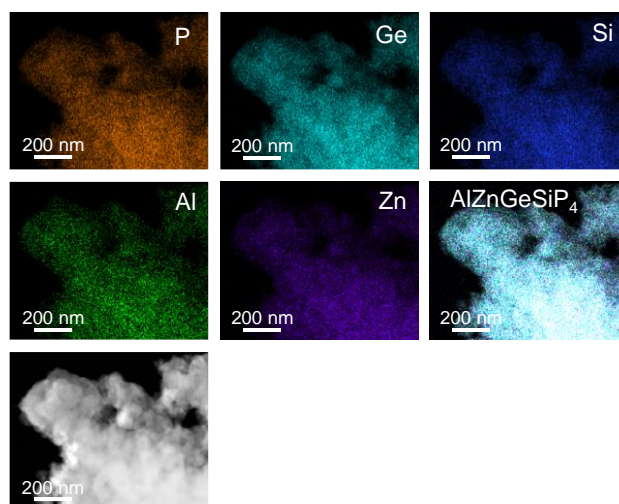
Figure S45. Elemental mappings of the sphalerite-structured GeP-based compound AlZnGeSiP$_4$.
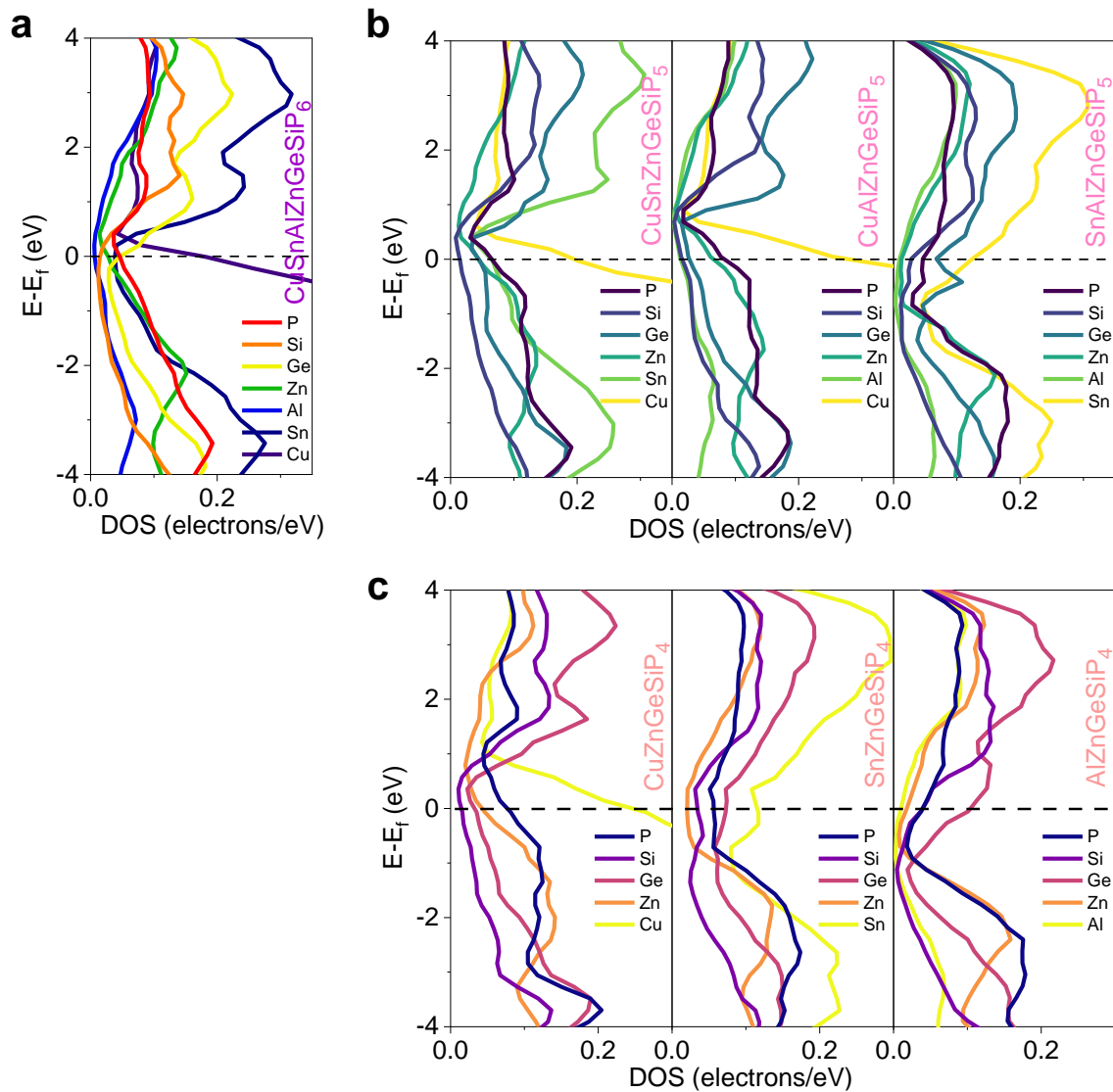
Figure S46. DOS of the high-entropy disordered-cation sphalerite-structured GeP-based compounds.

(a) Sphalerite-structured GeP-based compound $CuSnAlZnGeSiP_6$.

(b) Sphalerite-structured GeP-based compounds of $CuSn$ (or Al)$ZnGeSiP_5$, and $SnAlZnGeSiP_5$.

(c) Sphalerite-structured GeP-based compounds of Cu (Sn or Al)$ZnGeSiP_4$.

Disordered-cation sphalerite-structured GeP-based compounds, including $CuSnAlZnGeSiP_6$, $CuSn(or\ Al)ZnGeSiP_5$, $SnAlZnGeSiP_5$, and Cu (Sn or Al)$ZnGeSiP_4$ with a cubic ZnS lattice, all exhibit non-zero DOS profiles, thereby demonstrating metallic conductivity.
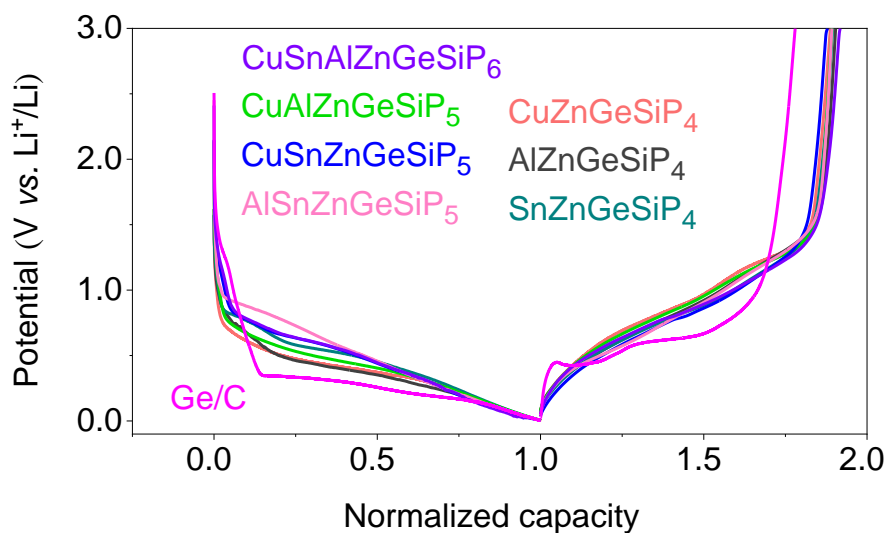
Figure S47. Normalized initial GCD profiles of the sphalerite-structured GeP-based compounds of CuSnAlZnGeSiP₆, CuSn (or Al)ZnGeSiP₅, SnAlZnGeSiP₅, and Cu (or Sn, or Al)ZnGeSiP₄; as well as Ge/C.
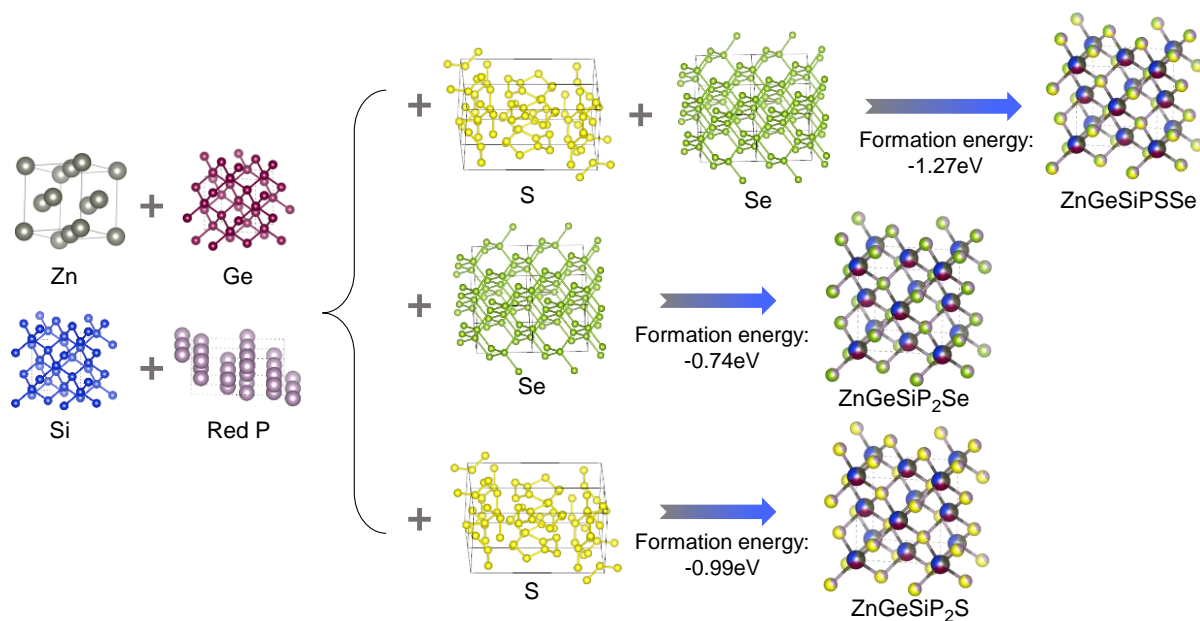
Figure S48. Structural diagram applied to calculate phase formation energies of disordered-cation and -anion sphalerite GeP-based compounds of ZnGeSiPSSe and ZnGeSiP₂Se (or S).
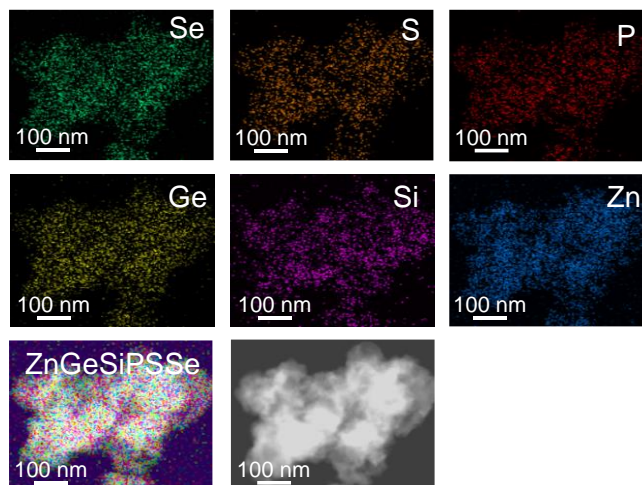
Figure S49. Elemental mappings of the sphalerite-structured GeP-based compound ZnGeSiPSSe.
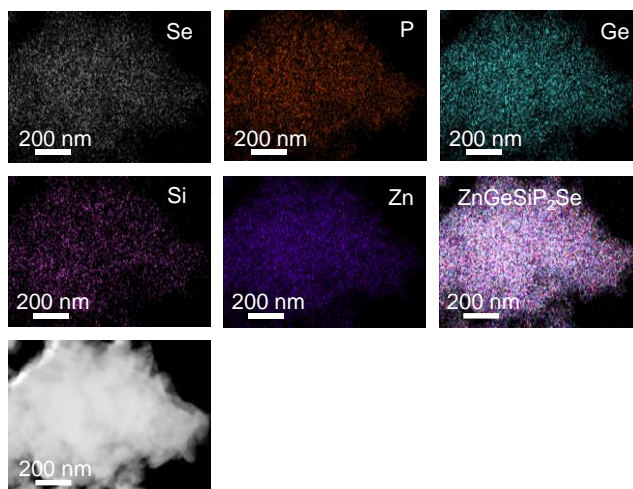
Figure S50. Elemental mappings of the sphalerite-structured GeP-based compound ZnGeSiP₂Se.
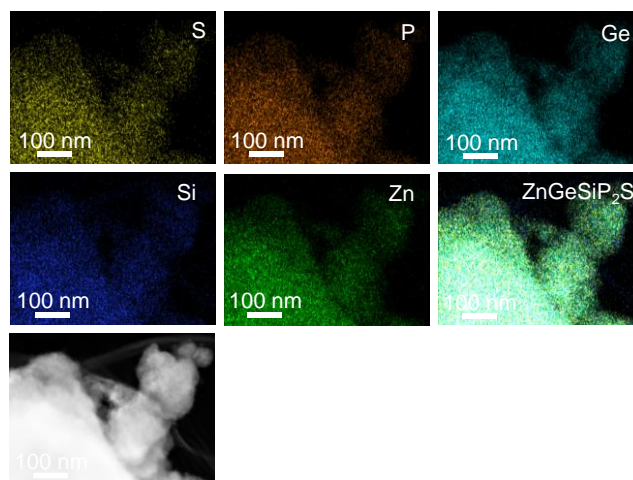
Figure S51. Elemental mappings of the sphalerite-structured GeP-based compound ZnGeSiP₂S.
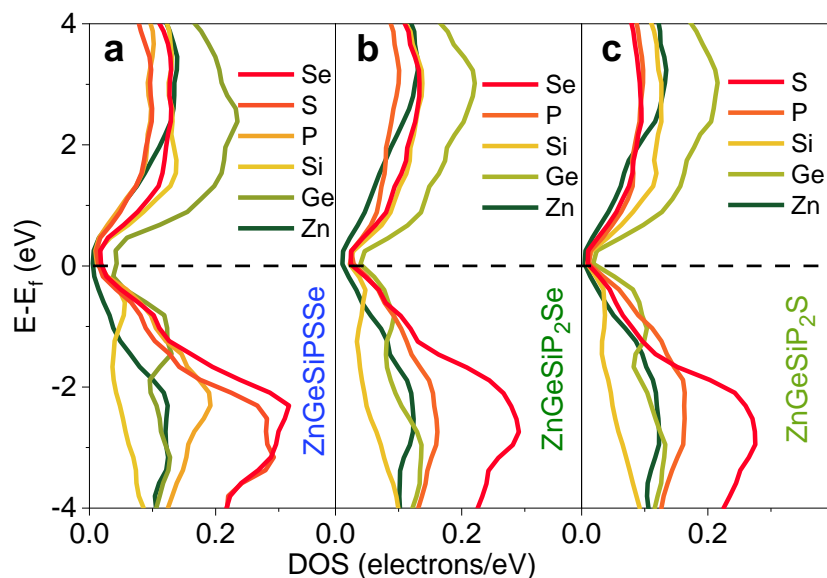
Figure S52. DOS for high-entropy sphalerite-structured GeP-based compounds, incorporating both mixed-cation and -anion components.
(a) ZnGeSiPSSe.
(b) ZnGeSiP$_2$Se.
(c) ZnGeSiP$_2$S.

Specifically, the sphalerite-structured GeP-based compounds, including ZnGeSiPSSe and ZnGeSiP$_2$Se (or S), exhibit non-zero DOS profiles, thereby attaining metallic conductivity.
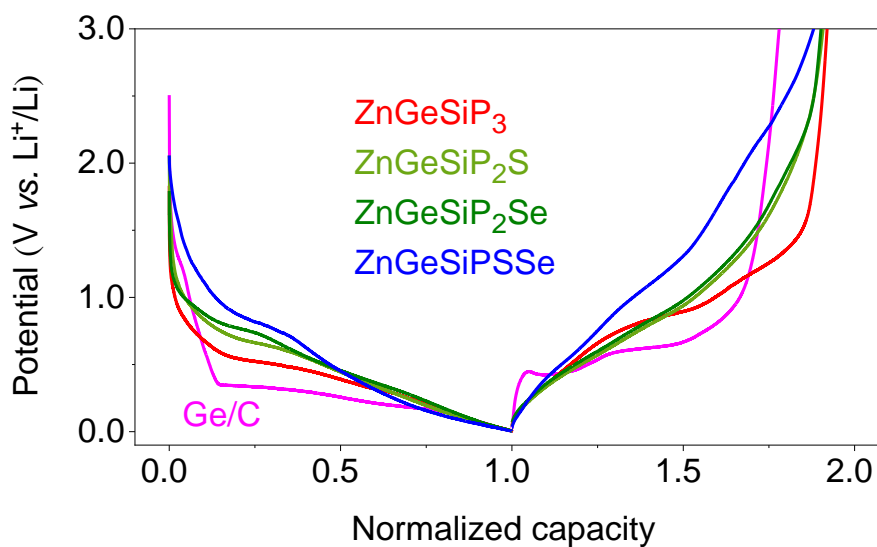
Figure S53. Normalized initial GCD profiles of the sphalerite-structured GeP-based compounds of ZnGeSiP$_3$, ZnGeSiPSSe, ZnGeSiP$_2$Se, and ZnGeSiP$_2$S; as well as Ge/C.

3. Supplementary Tables:

Table S1. Fractional atomic coordinates and isotropic displacement parameters for the monophasic $ZnGeSiP_3$ compound.

	X	Y	Z	O_{CC}
Zn	0	0	0	1/3
Ge	0	0	0	1/3
Si	0	0	0	1/3
P	0.25	0.25	0.25	1

Table S2. Main parameters of processing, and refinement of the sphalerite-structured GeP-based compound $ZnGeSiP_3$.

Compound	$ZnGeSiP_3$
Crystal System	Cubic
Space Group	F-43m
A, Å	a=5.436
2θ-interval, °	10-130
Rwp, %	2.65
Rp, %	1.97
χ^2	2.9

Table S3. Binding energy of the sphalerite-structured GeP-based compound $ZnGeSiP_3$ and the raw materials of Zn+Ge+Si+3P.

	Zn		Ge		Si		P	
$ZnGeSiP_3$	1045.7	1022.4	30.45	29.75	100.8	100.05	129.9	129.0
Raw materials	1045.2	1021.9	29.9	29.22	99.55	98.9	130.12	129.2
Shift	0.5	0.5	0.55	0.53	1.25	1.15	-0.22	-0.2

Table S4. Initial Coulombic efficiency (ICE), cyclic stability and rate performance for the sphalerite-structured GeP-based compound $ZnGeSiP_3$@Carbon composite, other Ge-, P-, or Si-based anodes reported recently.

Materials	ICE	Cycle performance	Rate performance	Reference
$ZnGeSiP_3$@Carbon	90.8%	2.0 A g^{-1}, 1600 cycles, 981 mA h g^{-1}	22 A g^{-1}, 568 mA h g^{-1}	This Work
Black Phosphorus	76%	5.2 A g^{-1}, 500 cycles, 790 mA h g^{-1}	13.0 A g^{-1}, 730 mA h g^{-1}	Science [11]
S-bridged phosphorus layer	-	1.05 A g^{-1}, 1500 cycles, 152 mA h g^{-1}	1.05 A g^{-1}, 160 mA h g^{-1}	Nat. Energy [12]
SiO_x@phosphorus	85.2%	1.5 A g^{-1}, 1000 cycles, 1050 mA h g^{-1}	4.5 A g^{-1}, 1450 mA h g^{-1}	EES [13]
Subnano-sized Si	90%	0.63 A g^{-1}, 50 cycles, 1125 mA h g^{-1}	6.3 A g^{-1}, 900 mA h g^{-1}	Nat. Energy [14]
Black phosphorus@Fe_3O_4	89.5%	2.0 A g^{-1}, 1000 cycles, 400 mA h g^{-1}	5.0 A g^{-1}, 376 mA h g^{-1}	Adv. Mater. [15]
Porous Si@carbon	80.3%	2.1 A g^{-1}, 1000 cycles, 679 mA h g^{-1}	8.4 A g^{-1}, 875 mA h g^{-1}	Nat. Commun. [16]
Graphene/Phosphorus	87.7%	1.3 A g^{-1}, 500 cycles, 1627 mA h g^{-1}	10.4 A g^{-1}, 1228 mA h g^{-1}	Adv. Mater. [17]
Porous Germanium	-	0.5 A g^{-1}, 200 cycles, 1345 mA h g^{-1}	10.0 A g^{-1}, 806 mA h g^{-1}	Adv. Energy Mater. [18]
Si-rich silicon nitride	89.5%	1.4 A g^{-1}, 200 cycles, 1998 mA h g^{-1}	19.7 A g^{-1}, 2370 mA h g^{-1}	EES [19]

$Ge_{1-x}Zn_xP$	-	1.0 A g^{-1}, 300 cycles, 900 mA h g^{-1}	2.0 A g^{-1}, 881 mA h g^{-1}	Adv. Energy Mater. [20]
SiO_x@carbon nanotube	77.9%	1.0 A g^{-1}, 200 cycles, 989 mA h g^{-1}	5.0 A g^{-1}, 500 mA h g^{-1}	EES [21]
Ge quantum dot/nitrogen-doped graphene	76.4%	1.6 A g^{-1}, 1000 cycles, 1200 mA h g^{-1}	16.0 A g^{-1}, 1001 mA h g^{-1}	Nat. Commun. [22]
Monoclinic phase GeP	88.8%	0.5 A g^{-1}, 350 cycles, 553 mA h g^{-1}	4.0 A g^{-1}, 330 mA h g^{-1}	Angew [23]
Li_3P-coated graphite	85%	0.16 A g^{-1}, 250 cycles, 275 mA h g^{-1}	1.92 A g^{-1}, 150 mA h g^{-1}	Adv. Mater. [24]
Si and carbon	89.6%	0.585 A g^{-1}, 300 cycles, 665 mA h g^{-1}	4.18 A g^{-1}, 407 mA h g^{-1}	Adv. Energy Mater. [25]
Modified black phosphorus	63.4%	0.26 A g^{-1}, 500 cycles, 281 mA h g^{-1}	10.4 A g^{-1}, 462 mA h g^{-1}	J. Am. Chem. Soc. [26]
Porous Si@MgF_2	86.2%	1.0 A g^{-1}, 200 cycles, 1403 mA h g^{-1}	5.0 A g^{-1}, 942 mA h g^{-1}	Adv. Funct. Mater. [27]
GeP-nanobar	87.0%	1.0 A g^{-1}, 500 cycles, 850 mA h g^{-1}	5.0 A g^{-1}, 620 mA h g^{-1}	Angew [28]
Red phosphorus	41%	1.0 A g^{-1}, 1200 cycles, 358 mA h g^{-1}	10.0 A g^{-1}, 200 mA h g^{-1}	Adv. Mater. [29]
sub-nano siliceous dots	-	1.0 A g^{-1}, 1000 cycles, 351 mA h g^{-1}	2.0 A g^{-1}, 362 mA h g^{-1}	Adv. Energy Mater. [30]
phosphorus/CNTs@reduced graphene oxide	83.8%	1.3 A g^{-1}, 100 cycles, 1725 mA h g^{-1}	26.0 A g^{-1}, 452 mA h g^{-1}	Chem [31]
Fe-Cu-Si ternary	91%	0.65 A g^{-1}, 50 cycles, 1500 mA h g^{-1}	-	EES [32]
Amorphous phosphorus@S, N co-doped carbon nanofibers	27.5%	0.1 A g^{-1}, 100 cycles, 567 mA h g^{-1}	2.0 A g^{-1}, 153 mA h g^{-1}	Adv. Energy Mater. [33]
$NiCoPS_3$@nitrogen-doped graphitized carbon	75.5%	0.5 A g^{-1}, 500 cycles, 784 mA h g^{-1}	5.0 A g^{-1}, 570 mA h g^{-1}	Adv. Energy Mater. [34]
ZnS/Sn@nitrogen-doped carbon	66.0%	0.1 A g^{-1}, 150 cycles, 769 mA h g^{-1}	6.0 A g^{-1}, 270 mA h g^{-1}	Adv. Funct. Mater. [35]
Phosphorus @SnO_2	64.4%	0.1 A g^{-1}, 100 cycles, 1189 mA h g^{-1}	1.0 A g^{-1}, 928 mA h g^{-1}	Nano Lett. [36]
Layered GeTe	80%	0.1 A g^{-1}, 300 cycles, 1021 mA h g^{-1}	2.0 A g^{-1}, 850 mA h g^{-1}	Energy Storage Mater. [37]

phosphorus@CNT-PAA/CMC	80%	1.3 A g^{-1}, 200 cycles, 1230 mA h g^{-1}	5.4 A g^{-1}, 1215 mA h g^{-1}	Adv. Funct. Mater. [38]
SiO$_x$@Single-walled CNT	81.5%	1.0 A g^{-1}, 200 cycles, 916 mA h g^{-1}	5.0 A g^{-1}, 311 mA h g^{-1}	Adv. Funct. Mater. [39]
Ge nanowire	81.4%	0.3 A g^{-1}, 300 cycles, 1059 mA h g^{-1}	3.0 A g^{-1}, 615 mA h g^{-1}	ACS Nano [40]
Porous silicon nanorods	60.7%	2.0 A g^{-1}, 300 cycles, 1539 mA h g^{-1}	8.0 A g^{-1}, 1565 mA h g^{-1}	ACS Nano [41]

Table S5. Theoretical volume expansion of the sphalerite-structured GeP-based compound ZnGeSiP$_3$, Ge, Si and P.

Materials	Theoretical volume expansion
ZnGeSiP$_3$	~256% (This work)
P	~300% (Li$_3$P)
Si	~392% (Li$_{22}$Si$_5$)
Ge	~350% (Li$_{22}$Ge$_5$)

Table S6. Fractional atomic coordinates, and isotropic displacement parameter of the single-phase sphalerite-structured GeP-based compound ZnGe$_2$P$_3$.

	X	Y	Z	O$_{CC}$
Zn	0	0	0	1/3
Ge	0	0	0	2/3
P	0.25	0.25	0.25	1

Table S7. Main parameters of processing, and refinement of the sphalerite-structured GeP-based compound $ZnGe_2P_3$.

Compound	$ZnGe_2P_3$
Crystal System	Cubic
Space Group	F -43m
A, Å	a=5.45
2θ-interval, °	10-120
Rwp, %	4.29
Rp, %	3.13
χ^2	2.01

4. Supplementary Movies:

Movie S1: Raman vibrations of the sphalerite-structured GeP-based compound $ZnGeSiP_3$.
Movie S2: Raman vibrations of the layer SiP.
Movie S3: Raman vibrations of the layer GeP.
Movie S4: Raman vibrations of the black P.

References:
1. Y. Yao, Z. Huang, P. Xie, S. D. Lacey, R. J. Jacob, H. Xie, F. Chen, A. Nie, T. Pu, M. Rehwoldt, D. Yu, M. R. Zachariah, C. Wang, R. Shahbazian-Yassar, J. Li and L. Hu, Carbothermal shock synthesis of high-entropy-alloy nanoparticles, *Science*, 2018, **359**, 1489-1494.
2. Y. Yao, Q. Dong, A. Brozena, J. Luo, J. Miao, M. Chi, C. Wang, I. G. Kevrekidis, Z. J. Ren, J. Greeley, G. Wang, A. Anapolsky and L. Hu, High-entropy nanoparticles: Synthesis-structure-property relationships and data-driven discovery, *Science*, 2022, **376**, eabn3103.

3. G. Cao, J. Liang, Z. Guo, K. Yang, G. Wang, H. Wang, X. Wan, Z. Li, Y. Bai, Y. Zhang, J. Liu, Y. Feng, Z. Zheng, C. Lu, G. He, Z. Xiong, Z. Liu, S. Chen, Y. Guo, M. Zeng, J. Lin and L. Fu, Liquid metal for high-entropy alloy nanoparticles synthesis, *Nature*, 2023, **619**, 73-77.

4. A. Nickol, T. Schied, C. Heubner, M. Schneider, A. Michaelis, M. Bobeth and G. Cuniberti, GITT analysis of lithium insertion cathodes for determining the lithium diffusion coefficient at low temperature: challenges and pitfalls, *J. Electrochem. Soc.*, 2020, **167**, 090546.

5. D. Kim, K. Zhang, M. Cho and Y.-M. Kang, Critical design factors for kinetically favorable P-based compounds toward alloying with Na ions for high-power sodium-ion batteries, *Energy Environ. Sci.*, 2019, **12**, 1326-1333.

6. G. Kresse and J. Furthmuller, Efficient iterative schemes for ab initio total-energy calculations using a plane-wave basis set, *Phys. Rev. B*, 1996, **54**, 11169-11186.

7. J. P. Perdew, K. Burke and M. Ernzerhof, Generalized Gradient Approximation Made Simple, *Phys. Rev. Lett.*, 1996, **77**, 3865-3868.

8. A. H. MacDonald, Comment on special points for Brillouin-zone integrations, *Phys. Rev. B*, 1978, **18**, 5897-5899.

9. X. Gonze, First-principles responses of solids to atomic displacements and homogeneous electric fields: Implementation of a conjugate-gradient algorithm, *Phys. Rev. B.*, 1997, **55**, 10337-10354.

10. G. Mills, H. Jónsson and G. K. Schenter, Reversible work transition state theory: application to dissociative adsorption of hydrogen, *Surf. Sci.*, 1995, **324**, 305-337.

11. H. Jin, S. Xin, C. Chuang, W. Li, H. Wang, J. Zhu, H. Xie, T. Zhang, Y. Wan, Z. Qi, W. Yan, Y. R. Lu, T. S. Chan, X. Wu, J. B. Goodenough, H. Ji and X. Duan, Black phosphorus composites with engineered interfaces for high-rate high-capacity lithium storage, *Science*, 2020, **370**, 192-197.

12. S. Tu, B. Zhang, Y. Zhang, Z. Chen, X. Wang, R. Zhan, Y. Ou, W. Wang, X. Liu, X. Duan, L. Wang and Y. Sun, Fast-charging capability of graphite-based lithium-ion batteries enabled by Li$_3$P-based crystalline solid–electrolyte interphase, *Nat. Energy*, 2023, **8**, 1365-1374.

13. K. Cheng, S. Tu, B. Zhang, W. Wang, X. Wang, Y. Tan, X. Chen, C. Li, C. Li, L. Wang and Y. Sun, Material–electrolyte interfacial interaction enabling the formation of an inorganic-rich solid electrolyte interphase for fast-charging Si-based lithium-ion batteries,

Energy Environ. Sci., 2024, **17**, 2631-2641.

14. J. Sung, N. Kim, J. Ma, J. H. Lee, S. H. Joo, T. Lee, S. Chae, M. Yoon, Y. Lee, J. Hwang, S. K. Kwak and J. Cho, Subnano-sized silicon anode via crystal growth inhibition mechanism and its application in a prototype battery pack, *Nat. Energy*, 2021, **6**, 1164-1175.

15. Y. Xiao, F. Liu, H. Shi, L. Hou, G. Qin, C. Yuan and X. W. D. Lou, Construction of ultrastable ultrathin black phosphorus nanodisks hybridized with Fe_3O_4 nanoclusters and iron(V)-oxo complex for efficient potassium storage, *Adv. Mater.*, 2023, DOI: 10.1002/adma.202301772, e2301772.

16. W. An, B. Gao, S. Mei, B. Xiang, J. Fu, L. Wang, Q. Zhang, P. K. Chu and K. Huo, Scalable synthesis of ant-nest-like bulk porous silicon for high-performance lithium-ion battery anodes, *Nat. Commun.*, 2019, **10**, 1447.

17. Y. Cao, S. Zhang, B. Zhang, C. Han, Y. Zhang, X. Wang, S. Liu, H. Gong, X. Liu, S. Fang, F. Pan and J. Sun, Local electric field promoted kinetics and interfacial stability of a phosphorus anode with ionic covalent organic frameworks, *Adv. Mater.*, 2023, **35**, e2208514.

18. S. Guo, Z. Sun, Y. Liu, X. Guo, H. Feng, S. Luo, C. Wei, Y. Zheng, X. Zhang, K. Kim, H. Liu, P. K. Chu, B. Gao, Q. Zhang and K. Huo, Multiscale micro-nano hierarchical porous germanium with self-adaptive stress dispersion for highly robust lithium-ion batteries anode, *Adv. Energy Mater.*, 2024, **14**, 2303876.

19. S. Chae, S. Park, K. Ahn, G. Nam, T. Lee, J. Sung, N. Kim and J. Cho, Gas phase synthesis of amorphous silicon nitride nanoparticles for high-energy LIBs, *Energy Environ. Sci.*, 2020, **13**, 1212-1221.

20. Y. Wei, R. Yao, Y. Zhao, R. Yang, J. Liu, X. Liu and H. Li, Triggering the phase conversion of GeP from monoclinic to cubic by Zn substitution toward a high-rate $Ge_{1-x}Zn_xP$ solid solution anode for Li-ion batteries, *Adv. Energy Mater.*, 2023, **13**, 2202884.

21. Z. He, C. Zhang, Y. Zhu and F. Wei, The acupuncture effect of carbon nanotubes induced by the volume expansion of silicon-based anodes, *Energy Environ. Sci.*, 2024, **17**, 3358-3364.

22. R. Mo, D. Rooney, K. Sun and H. Y. Yang, 3D nitrogen-doped graphene foam with encapsulated germanium/nitrogen-doped graphene yolk-shell nanoarchitecture for high-performance flexible Li-ion battery, *Nat. Commun.*, 2017, **8**, 13949.

23. T. Zeng, H. He, H. Guan, R. Yuan, X. Liu and C. Zhang, Tunable hollow nanoreactors for

in situ synthesis of GeP electrodes towards high-performance sodium ion batteries, *Angew. Chem. Int. Ed.*, 2021, **60**, 12103-12108.

24. Y. Huang, C. Wang, H. Lv, Y. Xie, S. Zhou, Y. Ye, E. Zhou, T. Zhu, H. Xie, W. Jiang, X. Wu, X. Kong, H. Jin and H. Ji, Bifunctional interphase promotes Li$^+$ de-solvation and transportation enabling fast-charging graphite anode at low temperature, *Adv. Mater.*, 2023, **36**, 2308675.

25. T. Lee, N. Kim, J. Lee, Y. Lee, J. Sung, H. Kim, S. Chae, H. Cha, Y. Son, S. K. Kwak and J. Cho, Suppressing deformation of silicon anodes via interfacial synthesis for fast-charging lithium-ion batteries, *Adv. Energy Mater.*, 2023, **13**, 2301139.

26. E. Zhou, X. Luo, H. Jin, C. Wang, Z. Lu, Y. Xie, S. Zhou, Y. Chen, Z. He, R. Ma, W. Zhang, H. Xie, S. Jiao, Y. Lin, D. S. Bin, R. Huang, X. Wu, X. Kong and H. Ji, Breaking low-strain and deep-potassiation trade-off in alloy anodes via bonding modulation for high-performance K-ion batteries, *J. Am. Chem. Soc.*, 2024, **146**, 4752-4761.

27. S. Mei, B. Xiang, S. Guo, J. Deng, J. Fu, X. Zhang, Y. Zheng, B. Gao, K. Huo and P. K. Chu, Design and electrochemical mechanism of the MgF$_2$ coating as a highly stable and conductive interlayer on the Si anode for high-performance Li-ion batteries, *Adv. Funct. Mater.*, 2023, **34**, 2301217.

28. T. Zeng, X. Liu, W. Kang, H. He, J. Zhang, X. Li and C. Zhang, In-situ templating growth of homeostatic GeP nano-bar corals with fast electron-ion transportation pathways for high performance Li-ion batteries, *Angew. Chem. Int. Ed.*, 2021, **60**, 26218-26225.

29. H. Yang, F. He, F. Liu, Z. Sun, Y. Shao, L. He, Q. Zhang and Y. Yu, Simultaneous catalytic acceleration of white phosphorus polymerization and red phosphorus potassiation for high-performance potassium-ion batteries, *Adv. Mater.*, 2024, **36**, e2306512.

30. Z. Liu, X. Wang, J. Hu, J. Meng, C. Niu, F. Liu, L. Cui, R. Yu and L. Mai, High-capacity sub-nano divalent silicon from biosilicification, *Adv. Energy Mater.*, 2023, **13**, 2301715.

31. J. Zhou, Z. Jiang, S. Niu, S. Zhu, J. Zhou, Y. Zhu, J. Liang, D. Han, K. Xu, L. Zhu, X. Liu, G. Wang and Y. Qian, Self-standing hierarchical P/CNTs@rGO with unprecedented capacity and stability for lithium and sodium storage, *Chem*, 2018, **4**, 372-385.

32. S. Chae, M. Ko, S. Park, N. Kim, J. Ma and J. Cho, Micron-sized Fe–Cu–Si ternary composite anodes for high energy Li-ion batteries, *Energy Environ. Sci.*, 2016, **9**, 1251-1257.

33. W. Feng, H. Wang, Y. Jiang, H. Zhang, W. Luo, W. Chen, C. Shen, C. Wang, J. Wu and L. Mai, A strain-relaxation red phosphorus freestanding anode for non-aqueous potassium

ion batteries, *Adv. Energy Mater.*, 2022, **12**, 2103343.

34. Q. Gui, Y. Feng, B. Chen, F. Gu, L. Chen, S. Meng, M. Xu, M. Xia, C. Zhang and J. Yang, Extrinsic-structured bimetallic-phase ternary metal phosphorus trisulfides coupled with N-doped graphitized carbon for superior electrochemical lithium storage, *Adv. Energy Mater.*, 2021, **11**, 2003553.

35. C. Ke, R. Shao, Y. Zhang, Z. Sun, S. Qi, H. Zhang, M. Li, Z. Chen, Y. Wang, B. Sa, H. Lin, H. Liu, M. S. Wang, S. Chen and Q. Zhang, Synergistic engineering of heterointerface and architecture in new-type ZnS/Sn heterostructures in situ encapsulated in nitrogen-doped carbon toward high-efficient lithium-ion storage, *Adv. Funct. Mater.*, 2022, **32**, 2205635.

36. C. Liu, M. Han, C. L. Chen, J. Yin, L. Zhang and J. Sun, Decorating phosphorus anode with SnO_2 nanoparticles to enhance polyphosphides chemisorption for high-performance lithium-ion batteries, *Nano Lett.*, 2023, **23**, 3507-3515.

37. X. Liu, Q. Ye, R. Yao, B. Chen, W. Liang, Y. Liu, Y. Liu, D. Chen, Y. Wei, D. Li and Y. Chen, Blue phosphorus-like layered GeTe for high rate and long cycle Li-ion batteries, *Energy Storage Mater.*, 2023, **63**, 103039.

38. M. Han, X. Liang, C. Han, C. Zhou, Q. Xiang, Y. Cao and J. Sun, Cross-linked binary polymeric binder of polyacrylic acid-carboxymethyl cellulose for improving phosphorus anode, *Adv. Funct. Mater.*, 2023, **34**, 2308325.

39. Z. He, Z. Xiao, H. Yue, Y. Jiang, M. Zhao, Y. Zhu, C. Yu, Z. Zhu, F. Lu, H. Jiang, C. Zhang and F. Wei, Single-walled carbon nanotube film as an efficient conductive network for Si-based anodes, *Adv. Funct. Mater.*, 2023, **33**, 2300094.

40. H. Liu, T. Wu, L. Zhang, X. Wang, H. Li, S. Liu, Q. Zhang, X. Zhang and H. Yu, Germanium nanowires via molten-salt electrolysis for lithium battery anode, *ACS Nano*, 2022, **16**, 14402-14411.

41. F. H. Du, Y. Ni, Y. Wang, D. Wang, Q. Ge, S. Chen and H. Y. Yang, Green fabrication of silkworm cocoon-like silicon-based composite for high-performance Li-ion batteries, *ACS Nano*, 2017, **11**, 8628-8635.